



The Dynamics of Elongated Earthquake Ruptures

Huihui Weng¹ and Jean-Paul Ampuero^{1,2}

¹Université Côte d'Azur, IRD, CNRS, Observatoire de la Côte d'Azur, Valbonne, France, ²Seismological Laboratory, California Institute of Technology, Pasadena, CA, USA

Key Points:

- An approximate rupture-tip-equation-of-motion for earthquakes with large rupture aspect ratio
- Long ruptures have inertia and their energy is limited by rupture width
- Definition of a rupture potential to assess the location of rupture arrest

Correspondence to:

H. Weng,
weng@geoazur.unice.fr

Citation:

Weng, H., & Ampuero, J.-P. (2019). The dynamics of elongated earthquake ruptures. *Journal of Geophysical Research: Solid Earth*, 124, 8584–8610. <https://doi.org/10.1029/2019JB017684>

Received 13 MAR 2019

Accepted 21 JUL 2019

Accepted article online 30 JUL 2019

Published online 14 AUG 2019

Abstract The largest earthquakes propagate laterally after saturating the fault's seismogenic width and reach large length-to-width ratios L/W . Smaller earthquakes can also develop elongated ruptures due to confinement by heterogeneities of initial stresses or material properties. The energetics of such elongated ruptures is radically different from that of conventional circular crack models: they feature width-limited rather than length-dependent energy release rate. However, a synoptic understanding of their dynamics is still missing. Here we combine computational and analytical modeling of long ruptures in three dimension (3D) and 2.5D (width-averaged) to develop a theoretical relation between the evolution of rupture speed and the along-strike distribution of fault stress, fracture energy, and rupture width. We find that the evolution of elongated ruptures in our simulations is well described by the following rupture-tip-equation-of-motion:

$$G_c = G_0 \left(1 - \frac{\dot{v}_r W}{v_s^2} \frac{\gamma}{A\alpha_s^p} \right) \quad (1)$$

where G_c is the fracture energy, G_0 is the steady state energy release rate, v_s is the S wave speed, v_r is the rupture speed, $\dot{v}_r = dv_r/dt$ is the rupture acceleration, and $\gamma/A\alpha_s^p$ is a known function of rupture speed. The steady energy release rate is limited by rupture width as $G_0 = \gamma\Delta\tau^2 W/\mu$, where γ is a geometric factor, $\Delta\tau$ is the stress drop (spatially smoothed over a length scale smaller than W), and μ is the shear modulus. If G_c is a constant and exactly balanced by G_0 , the rupture can in principle propagate steadily at any speed. If G_c increases with rupture speed, steady ruptures have a well-defined speed and are stable. When $G_c \neq G_0$, the rupture acquires an inertial effect: the rupture-tip-equation-of-motion depends explicitly on rupture acceleration. This inertial effect does not exist in the classical theory of dynamic rupture in 2-D unbounded media and in unbounded faults in 3D, but emerges in 2-D bounded media or, as shown here, as a consequence of the finite rupture width in 3D. These findings highlight the essential role of the seismogenic width on rupture dynamics. Based on the rupture-tip-equation-of-motion we define the rupture potential, a function that determines the size of next earthquake, and we propose a conceptual model that helps rationalize one type of “supercycles” observed on segmented faults. More generally, the theory developed here can yield relations between earthquake source properties (final magnitude, moment rate function, radiated energy) and the heterogeneities of stress and strength along the fault, which can then be used to extract statistical information on fault heterogeneity from source time functions of past earthquakes or as physics-based constraints on finite-fault source inversion and on seismic hazard assessment.

1. Introduction

Elucidating what controls earthquake rupture speed has significant implications for understanding earthquake physics and seismic radiation. The theory of linear elastic fracture mechanics (LEFM; Aki & Richards, 2002; Freund, 1998; Kostrov, 1964; Madariaga, 1983) provides a fundamental framework to predict the propagation of ruptures in basic two-dimensional (2-D) problems, via a crack-tip-equation-of-motion that relates rupture length, L , to its first derivative, rupture speed, $v_r = dL/dt$. It takes the form of the following energy flux balance equation:

$$G_c = G(v_r, L, \Delta\tau) \quad (2)$$

where G is the energy release rate, defined as the energy flux from the elastic medium to the crack tip per unit of crack tip advance, and G_c is the fracture energy dissipated in the vicinity of the

rupture front. This differential equation has been crucial to conceptually understand the first-order controls on the evolution of rupture in 2-D earthquake models (Aki & Richards, 2002; Burridge, 1973; Freund, 1979) and in laboratory experiments (Kammer et al., 2018; Svetlizky et al., 2017; Svetlizky & Fineberg, 2014).

However, the 2-D crack-tip-equation-of-motion may be inadequate for large crustal earthquakes in 3D whose rupture length exceeds the seismogenic width (Figure 1a). Whereas in 2D the energy release rate grows linearly with rupture length, in 3-D elongated faults the interaction between the rupture and the seismogenic boundaries makes the energy release rate dependent on rupture width rather than rupture length (Dalguer & Day, 2009; Day, 1982; Weng & Yang, 2017). For example, 3-D numerical simulations have shown that whether a long rupture is self-arresting or runaway depends on seismogenic width, fault stress, and frictional parameters, but not on rupture length (Weng & Yang, 2017). Elongated rupture models of large earthquakes have been classically considered in seismology (Haskell, 1964) and offer one plausible explanation for observations of source spectra with two corner frequencies in teleseismic analyses (e.g., Denolle & Shearer, 2016). The second corner frequency, if related to the risetime of slip, can have a lower bound dictated by the seismogenic width (Day, 1982; Savage, 1972). Elongated rupture models are also considered in the context of earthquake moment-area scaling relations (Luo et al., 2017) and moment-duration scaling of slow and regular earthquakes (Gomberg et al., 2016).

Elongated ruptures can happen also in moderate earthquakes (Figure 2) and even in small earthquakes, as suggested by spectra with double corner frequencies (Imanishi & Ellsworth, 2006; Uchide & Imanishi, 2016) and source inversion studies (Okuda & Ide, 2018). The rupture width of moderate and small earthquakes may be confined by other constraints such as heterogeneities of initial stresses and fault materials. An example is the 2004 M_w 6 Parkfield earthquake, whose rupture depth extent is about 6 km and aspect ratio is between 3 and 5 (Custódio et al., 2005; Uchide & Ide, 2010). Ruptures nucleated near the bottom of the seismogenic zone can remain confined at depth without breaking the entire seismogenic width due to the decaying stress available in shallower areas if the fault is loaded from the bottom by deep fault creep. This interpretation has been proposed for the 2015 M_w 7.8 Gorkha, Nepal earthquake (Avouac et al., 2015; Michel et al., 2017).

Elongated ruptures may play an important role also in induced seismicity. Rupture width may be confined to the intersection of a fault and a fluid reservoir if there are unfavorable stresses or velocity-strengthening fault materials outside the fluid-injection layer (Galis et al., 2017; Galis et al., 2018). In producing gas fields, the rupture width of induced earthquakes may be limited by the width of stress concentrations along the top or bottom of a fault/reservoir intersection caused by differential compaction between the reservoir compartments offset by the fault (e.g., Buijze et al., 2019).

In contrast to equation (2), if the 2-D elastic medium has a finite width W in the crack-normal direction and the crack is longer than W , the energy release rate is length-independent (Goldman et al., 2010; Marder, 1998). In this so-called “strip configuration”, an approximate crack-tip-equation-of-motion is (Marder, 1998)

$$G_c = G_0 \left(1 - \frac{\dot{v}_r W}{v_p^2} \frac{1}{2\alpha_R^4} \right) \quad (3)$$

where G_0 is the steady state energy release rate, $\dot{v}_r = dv_r/dt$ is the crack acceleration, v_p is the P wave speed, $\alpha_R = \sqrt{1 - (v_r/v_R)^2}$, and v_R is the Rayleigh speed. The steady energy release rate does not depend on rupture length; it is $G_0 = \gamma \Delta\tau^2 W / \mu$, where $\Delta\tau$ is the stress drop, μ is the shear modulus, and γ is a geometric factor of order 1. Equation (3) was developed under the assumption that the crack accelerates slowly, $W\dot{v}_r/v_p^2 \ll 1$; that is, its speed changes little over the time scale of propagation of waves up to the boundaries. The equation has been validated by laboratory experiments of mode I crack in the strip configuration (Goldman et al., 2010). In contrast to equation (2) in 2-D unbounded media, equation (3) features an “inertial effect”: it depends explicitly on crack acceleration.

Here we demonstrate that 3-D elongated ruptures obey a rupture-tip-equation-of-motion similar to that of the 2-D strip-crack problem. To enable mathematical tractability and affordable computational cost, we

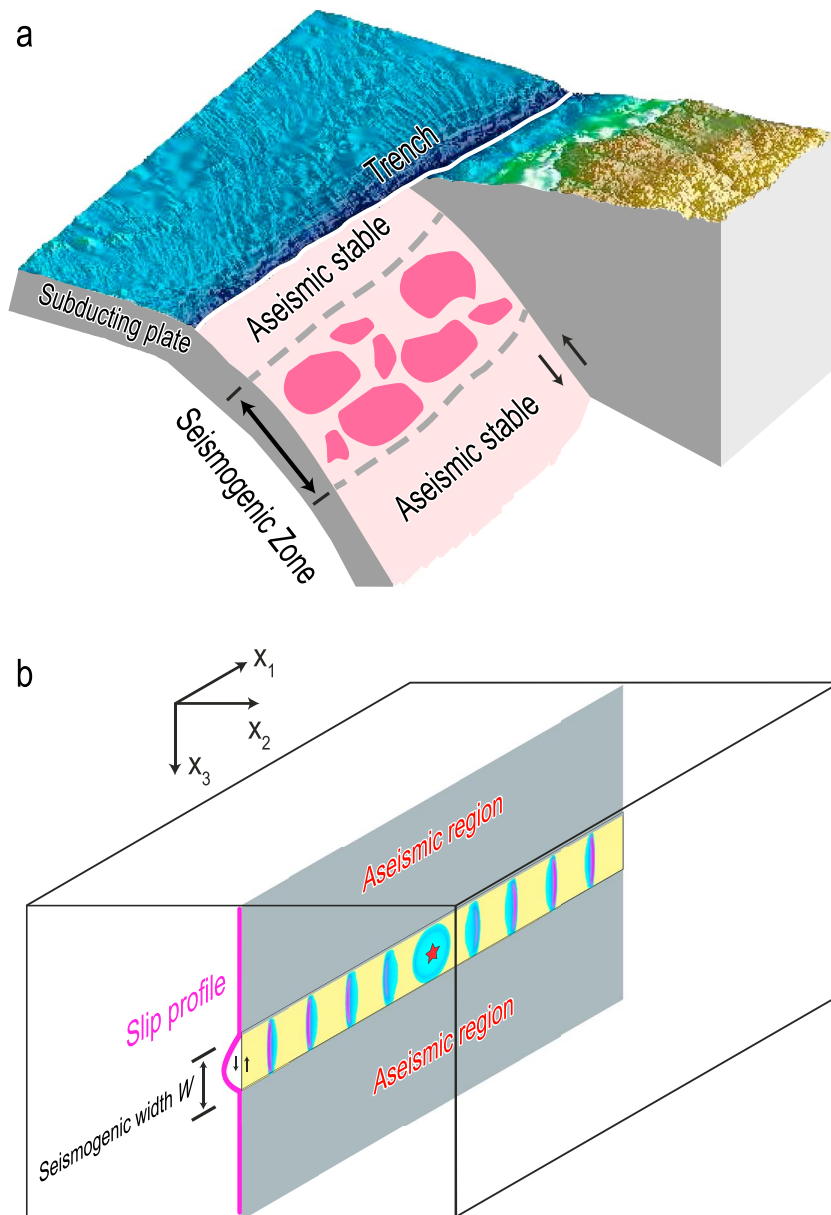


Figure 1. (a) A subduction zone megathrust with seismic and aseismic zones, including heterogeneities in the seismogenic zone. (b) Antiplane (mode III) rupture model along a planar dip-slip fault with finite seismogenic width (yellow region) in an unbounded elastic medium. The red star marks the hypocenter. The patches inside the yellow region are snapshots of slip rate at different times, illustrating a typical pulse-like rupture due to the seismogenic boundaries. The gray regions are aseismic zones (no coseismic slip). The pink curve shows the slip profile across the depth.

study systematically a reduced-dimensionality (2.5-D) model that accounts approximately for the finite rupture width. Our 2.5-D results are then validated by a selected set of 3-D dynamic rupture simulations on very long faults. We find that the rupture-tip-equation-of-motion similar to equation (3) describes well the dynamics of elongated ruptures in 2.5-D and 3-D simulations. To illustrate how this theoretical result provides valuable insight into earthquake physics, we analyze its implications for the stability of rupture speed, including rupture arrest, to heterogeneities of fracture energy and initial fault stress. We also discuss implications of the theory for physics-based hazard assessment and for inferences of fault mechanical properties from geophysical observations.

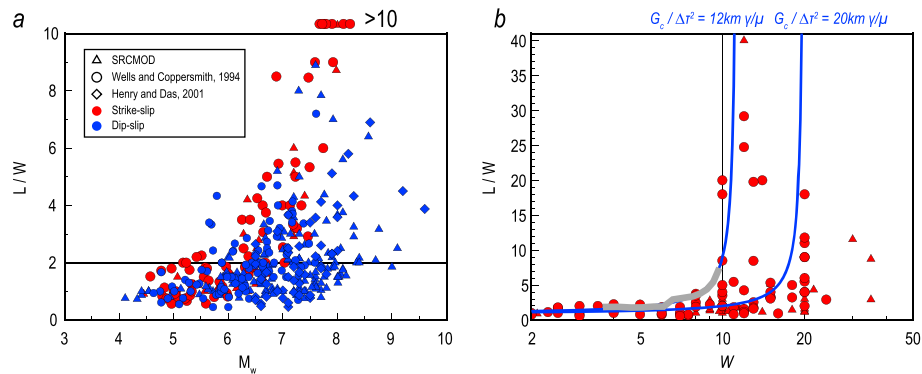


Figure 2. (a) Aspect ratio L/W versus moment magnitude for global earthquakes, from the catalogs of Wells and Coppersmith (1994), Henry and Das (2001), and the online SRCMOD database (Mai & Thingbaijam, 2014). (b) Aspect ratio versus seismogenic width W for strike-slip earthquakes. The thin black vertical line marks the critical width of strike-slip catalogs, above which ruptures with very high aspect ratios have occurred. The gray curve is the result of 3-D dynamic rupture simulations by Weng and Yang (2017) and the blue curves are derived in this paper assuming two different values of the critical width $W_c = \mu G_c / \gamma \Delta\tau^2 = 12$ km and 20 km, respectively.

2. Theoretical and Numerical Models

2.1. Problem Statement in 3D

Our general goal is to gain theoretical insight into the dynamics of elongated earthquake ruptures. To facilitate mathematical and computational analysis while preserving the essence of the real problem, we make here a number of simplifying assumptions. We consider a vertical fault of infinite length and finite width W , embedded in a 3-D unbounded, homogeneous, linear elastic medium (Figure 1b). The shear modulus and S wave speed of the medium are denoted μ and v_s , respectively. To avoid the complications of supershear ruptures (propagating faster than S wave speed) that can occur in long strike-slip faults, in this study we focus on dip-slip faulting. We adopt a Cartesian coordinate system in which x_3 denotes depth. The fault is located on the $x_2 = 0$ plane and has a strike parallel to x_1 and slip parallel to x_3 .

We assume that slip and tractions on the fault are related by a friction law with finite fracture energy G_c , which may be a material property or depend on local fault variables such as slip or slip velocity. Our work combines theory and modeling, and in each approach friction is described with a different level of detail. Our theoretical analysis is within the small scale yielding regime of fracture mechanics, in which the size of the process zone near the rupture front is small compared to other length scales of the problem. In such regime, fracture energy is an essential parameter and the details of the friction law are of secondary importance. In contrast, in our numerical simulations a specific friction law must be prescribed. To have full control on the fracture energy in our simulations, we assume that the fault is governed by the linear slip-weakening friction law (Andrews, 1976a, 1976b; Freund, 1979; Ida, 1972). The fault normal stress is time-independent owing to the symmetries of the problem, and the frictional strength parameters prescribed are the static strength τ_s , the dynamic strength τ_d , and the slip-weakening distance d_0 . The fracture energy is $G_c = 0.5(\tau_s - \tau_d)d_0$. The nominal stress drop is $\Delta\tau = \tau_0 - \tau_d$ and τ_0 is the initial shear stress; the real stress drop in simulations is slightly different due to overshoot or undershoot effects.

Large ruptures nucleate at depth, then reach the fault width, and continue their propagation laterally as bilateral slip pulses (Ampuero & Mao, 2017; Day, 1982). The focus of our work is on the later stage of lateral pulse-like rupture. For simplicity, in our numerical simulations we consider only symmetric ruptures, but this is not a strong assumption because in fast bilateral pulse-like ruptures the two fronts do not interact.

2.2. Reduction to a 2.5-D Model

The 3-D problem is approximated here by a reduced-dimensionality (2.5-D) model (Appendix A.1.). There are two interpretations of the 2.5-D model: the Elsasser's model and the Fourier transform analogy. Whereas the latter is our preferred interpretation and our original contribution, we mention the former mostly for historical reasons.

A 2.5-D Elsasser-type formulation was developed for quasi-static faulting in an elastic layer over a viscoelastic half-space by Rice (1980) and Lehner et al. (1981). The approach involves variables and momentum equations averaged across the thickness of the elastic layer, analogous to the shallow water approximation for tsunami waves. It was extended to dynamic faulting by Johnson (1992) to study the effect of lithospheric thickness on earthquake rupture. For purely elastic media (without viscosity), a scalar version of the 2.5-D equations for strike-slip faulting was introduced by Lapusta (2001) and used in dynamic rupture studies under the name of “crustal plane model” (e.g., Appendix A of Kaneko and Lapusta (2008)). Similar 2.5-D governing equations were used in earthquake cycle models (Langer et al., 1996; Myers et al., 1996) and to study the effect of seismic width on the growth and evolution of fault systems and on the earthquakes they produce (Shaw, 2004; Spyropoulos et al., 2002).

In Appendix A.1. we propose an alternative derivation of a 2.5-D model in which, rather than depth-averaging, we consider a scalar wave equation and isolate a single vertical Fourier mode as a crude way to account for the constrained depth profile of slip. The resulting 2.5-D governing equation is

$$\frac{\partial^2 u}{\partial x_1^2} + \frac{\partial^2 u}{\partial x_2^2} - \frac{u}{(\gamma W)^2} = \frac{1}{v_s^2} \frac{\partial^2 u}{\partial t^2} \quad (4)$$

where u is the displacement and γ is a coefficient that depends on the assumed depth distribution of slip. For a fault embedded in an unbounded space, approximating the depth profile of slip as one half of a cosine of wavelength $2W$ leads to $\gamma = 1/\pi$. In a shallow fault on a half-space, $\gamma = 2/\pi$. For a buried fault the value of γ is between $1/\pi$ and $2/\pi$. Equation (4) is known as the Klein-Gordon equation in physics and a similar equation (Carlson et al., 1994) was introduced independently as the continuous limit of the Burridge-Knopoff model.

The 2.5-D model is convenient for two reasons. Compared to the 2-D antiplane wave equation, the only difference in equation (4) is the additional term $u/(\gamma W)^2$. This similarity of governing equations makes it possible to study theoretically the 2.5-D problem by exploiting 2-D results. Moreover, the 2.5-D approach enables numerical simulations that approximately account for the 3-D effect of a finite rupture depth at the same computational cost as a 2-D simulation.

For convenience, we define a reduced rupture width:

$$W' = \gamma W \quad (5)$$

2.3. Energy Release Rate of a Steady State Rupture

We first consider a semiinfinite rupture propagating at constant speed. We assume a uniform stress drop, $\Delta\tau$, for $0 < x < L$, and zero stress drop for $x < 0$. The near-tip stresses $\Delta\sigma_{ij}$ in the 2.5-D model have the same asymptotic form as in the 2-D mode III crack problem (Appendix A.3.):

$$\Delta\sigma_{ij}(r, \theta) \approx \frac{K_{III}(v_r)}{\sqrt{2\pi r}} \Sigma_{ij}^{III}(\theta, v_r) \quad (6)$$

where r and θ are the distance and azimuth in the polar coordinates centered at the rupture tip, K_{III} is the stress intensity factor, and Σ_{ij}^{III} is a known universal function (Freund, 1998). The energy release rate is (Appendix A.3.)

$$G = \frac{1}{2\mu} g(v_r) K_{III}^2(v_r) \quad (7)$$

where

$$g(v_r) = \frac{1}{\alpha_s} \quad (8)$$

and $\alpha_s = \sqrt{1 - (v_r/v_s)^2}$. The stress intensity factor is related to stress drop and rupture length, width, and speed by (Appendix A.2.)

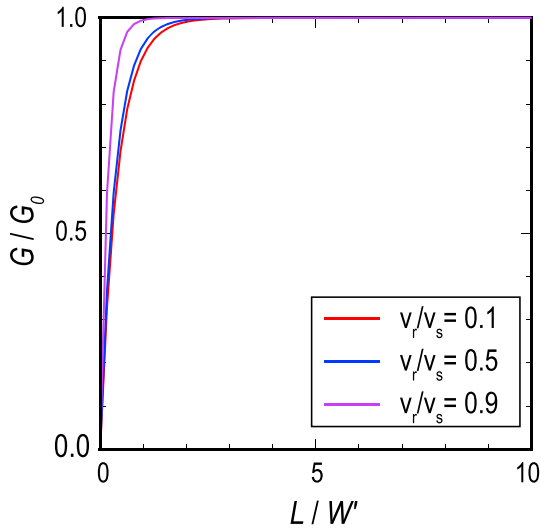


Figure 3. The ratio between dynamic and steady energy release rates (the function f in equation (10)) for different values of normalized rupture length L/W' and speed v_r/v_s .

$$K_{III}(v_r) = \Delta\tau[2\alpha_s W']^{1/2} \cdot \text{erf} \left\{ \left[\frac{1}{\alpha_s} \frac{L}{W'} \right]^{1/2} \right\} \quad (9)$$

where erf is the error function. Our conclusions do not depend strongly on the assumed spatial distribution of stress drop. In fact, the dependence of $K_{III}(v_r)$ on an arbitrary spatially variable stress drop, $\Delta\tau(x)$ (Appendix A.2.), involves a weight function that decays steeply behind the rupture tip over a short distance $W' \alpha_s$ comparable to the pulse size. Substituting equations (8) and (9) into equation (7), the resulting energy release rate is

$$G = G_0 f(L/W', v_r/v_s) \quad (10)$$

where

$$G_0 = \frac{\Delta\tau^2 W'}{\mu} \quad (11)$$

and

$$f(L/W', v_r/v_s) = \text{erf}^2 \left\{ \left[\frac{1}{\alpha_s} \frac{L}{W'} \right]^{1/2} \right\} \quad (12)$$

The function f grows quickly from 0 to 1 as the normalized rupture length L/W' increases. For a bilateral rupture with half-length L such that $L/W' > 2$, $f \approx 1$ for different values of v_r/v_s (Figure 3), and thus $G \approx G_0$. Hence, G_0 is the steady state energy release rate, regardless of rupture speed and propagation distance.

2.4. Numerical Models

We use both 3-D and 2.5-D dynamic rupture simulations to investigate the evolution of earthquake rupture speed on elongated faults. As the computational cost is much lower in 2.5D than in 3D, we consider much longer faults and study the problem more systematically in the 2.5-D model. In both type of simulations, to avoid the effects of waves reflected from the model boundaries, we consider a large domain and simulation times shorter than the time required for the earliest seismic waves to reflect from the model boundaries and travel back to the fault. In the 2.5-D simulations, considering the symmetries of the problem, the computational domain is restricted to a quarter of the actual model domain. In the 3-D simulations, we assume a Poisson's ratio of 0.25. The values of other material properties are not important because we present results in nondimensional form.

Our simulations span a wide range of length scales. The smallest length scale of the problem is the cohesive zone size Λ . For the slip-weakening friction law in the 2-D antiplane model it can be estimated by (Day et al., 2005)

$$\Lambda = \alpha_s \Lambda_0; \Lambda_0 = \frac{9\pi \mu d_0}{32 \tau_s - \tau_d} \quad (13)$$

where Λ_0 is the static cohesive zone size. The cohesive zone size in the 2.5-D model is the same as in the 2-D model. The propagation of a rupture with finite cohesive length can be approximated by LEFM when the cohesive zone size is much smaller than the dimensions of the rupture, $\Lambda \ll W$ and $\Lambda \ll L$. To guarantee sufficient numerical resolution, the grid size Δx is set much smaller than the static cohesive zone size, $\Delta x \ll \Lambda_0$. Thus, our simulations require the condition $\Delta x \ll \Lambda_0 \ll W \ll L$. In 2.5D, we choose the parameters and grid size to ensure $\Lambda_0/\Delta x = 32$, to test different ratios of W/Λ_0 between 1 and 30, and to test the largest model with $L/W = 60$. In 3D, we set $W/\Lambda_0 = 5$ and $\Lambda_0/\Delta x = 16$, and our largest model has $L/W = 10$.

The simulations are based on the spectral element method (Ampuero, 2002; Komatitsch & Vilotte, 1998) for the spatial discretization and on the explicit Newmark method for the time discretization. For 2.5-D simulations we use the software SEMLAB (<https://github.com/jpampuero/semlab>) in Matlab on a single processor, with vectorization optimizations. For 3-D simulations we use the software

SPECFEM3D (<https://geodynamics.org/cig/software/specfem3d/>) with the implementation of fault dynamics by Kaneko et al. (2008) and Galvez et al. (2014) on a medium-scale computing cluster with 64 cores and 384-GB memory in each node. The time step is set according to the Courant-Friedrichs-Lewy stability condition.

We initiate the ruptures at the fault center by imposing a time weakening of the friction coefficient (Andrews, 1985) over a region expanding at speed $0.1 v_s$, up to a distance $L/W = 2$. Eventually, rupture propagation becomes spontaneous and accelerates, driven by slip weakening. Immediate fault healing is assumed in 2.5D (the friction coefficient is restored to its static value when slip rate becomes zero), but not in 3D (the friction coefficient remains at its dynamic value even after slip arrest).

3. Results

3.1. Rupture Acceleration Phase in 2.5D

We ran a set of 2.5-D simulations assuming a spatially uniform ratio of fracture energy to steady energy release rate, G_c/G_0 . This energy ratio is the same (except for the geometric coefficient γ) as the nondimensional parameter κ introduced by Madariaga and Olsen (2000). After nucleation, ruptures accelerate toward the S wave speed if $G_c/G_0 < 1$ (Figure 4a). The value of the energy ratio controls the rupture evolution: the smaller it is, the faster the rupture accelerates.

We hypothesize that the rupture-tip-equation-of-motion along a depth-bounded fault in 2.5D has the following form, similar to equation (3) in the strip configuration:

$$G_c = G_0 \left(1 - \frac{\dot{v}_r W'}{v_s^2} \frac{1}{A \alpha_s^P} \right)$$

where v_s is the S wave speed (the limiting speed in mode III), $\alpha_s = \sqrt{1 - (v_r/v_s)^2}$, and A and P are two constants to be determined. To test our hypothesis, we rewrite the equation as

$$\frac{\dot{v}_r W'}{v_s^2 (1 - G_c/G_0)} = A \alpha_s^P \quad (14)$$

After normalizing the rupture acceleration \dot{v}_r by $v_s^2 (1 - G_c/G_0) / W'$, we find that all the acceleration versus speed curves obtained in our simulations collapse onto a single curve (Figure 4b). We determine that the best fitting values in the least squares sense are $A = 1$ and $P = 3$. Considering that the function α_s^3 approaches 0 for large rupture speed, we compare its inverse $1/\alpha_s^3$ with the numerical results and find remarkable agreement (Figure 5). The acceleration phases of all the models with $G_c/G_0 < 1$ are thus well predicted by the equation

$$\frac{\dot{v}_r W'}{v_s^2 (1 - G_c/G_0)} = \alpha_s^3 \quad (15)$$

and the energy balance is well approximated by

$$G_c = G_0 \left(1 - \frac{\dot{v}_r W'}{v_s^2} \frac{1}{\alpha_s^3} \right) \quad (16)$$

For steady ruptures (when $\dot{v}_r = 0$) equation (16) yields $G_c = G_0$, consistently with our previous statement that G_0 is the steady energy release rate. Remarkably, G_0 does not depend on rupture speed and, in particular, it is also the static energy release rate (at zero speed). In contrast, the energy release rate of steady ruptures in unbounded 2-D media depends strongly on rupture speed, for all rupture types including self-similar cracks (Freund, 1998), self-similar pulses (Nielsen & Madariaga, 2003), and steady state pulses (Rice et al., 2005).

For nonsteady ruptures, if $G_0 > G_c$, the “inertial term” of the right-hand side is nonzero and provides a positive acceleration. As the rupture speed approaches the S wave speed, the function α_s approaches 0 and equation (15) shows that the acceleration \dot{v}_r vanishes too. The rupture-tip-equation-of-motion

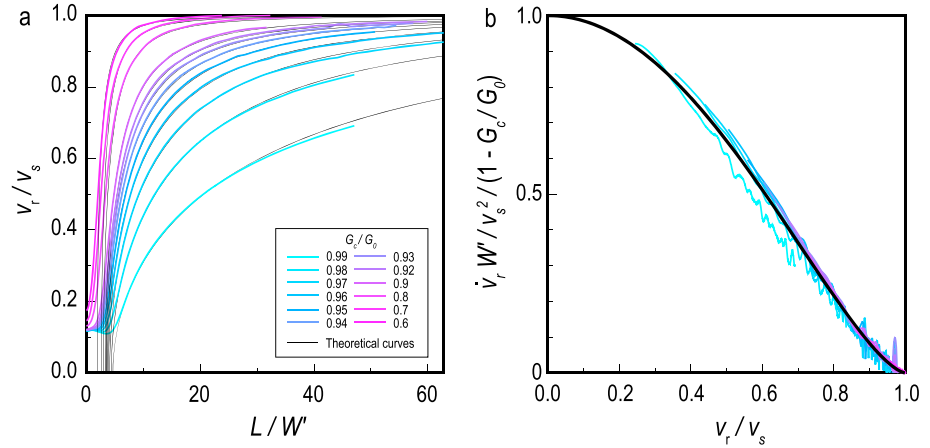


Figure 4. (a) Normalized rupture speed (colored curves coded by G_c/G_0) as a function of normalized distance from the 2.5-D numerical simulations versus theoretical estimation (black thin curves). (b) Normalized rupture acceleration as a function of normalized rupture speed, compared with the theoretical estimation.

(equation (15)) does not depend explicitly on the rupture distance L , unlike the case of a 2-D unbounded medium (equation (2)).

3.2. Spatial Distribution of Rupture Speed Under Uniform Energy Ratio

Assuming that G_c/G_0 is constant, the relation between rupture speed and propagation distance can be determined analytically in closed form. Equation (15) can be written in the following differential form:

$$\frac{(1-G_c/G_0)}{W'} dt = \frac{dv_r}{v_s^2 \alpha_s^3} \quad (17)$$

Multiplying by v_r both sides of equation (17), considering $dL = v_r dt$, and integrating we get

$$(1-G_c/G_0)(L_1-L_2)/W' = \alpha_{s1}^{-1} - \alpha_{s2}^{-1} \quad (18)$$

where L_1 and L_2 are two arbitrary rupture front positions along the fault and α_{s1} and α_{s2} are the functions of rupture speed α_s at the positions L_1 and L_2 . Choosing a reference position L_1 at which the rupture speed is known, equation (18) gives a relation between rupture speed v_r and propagation distance L .

We find this approach fits well the simulation results (Figure 4a) in the well-developed rupture acceleration phase. Each predicted curve in Figure 4a intercepts the horizontal axis (zero rupture speed), at a rupture length defined as L_0 . This is not a fixed characteristic length of the problem, but depends on details of the nucleation process (Figure 6a). If the nucleation is vigorous, for instance if the prescribed nucleation speed is high, the rupture reaches a high speed inside the nucleation zone quickly and thus has a shorter L_0 . Choosing L_0 as the reference position, setting $L_1 = L_0$, $\alpha_{s2} = 1$, and $L_2 = L$ in equation (18), we get

$$(1-G_c/G_0)(L-L_0)/W' = \alpha_s^{-1} - 1 \quad (19)$$

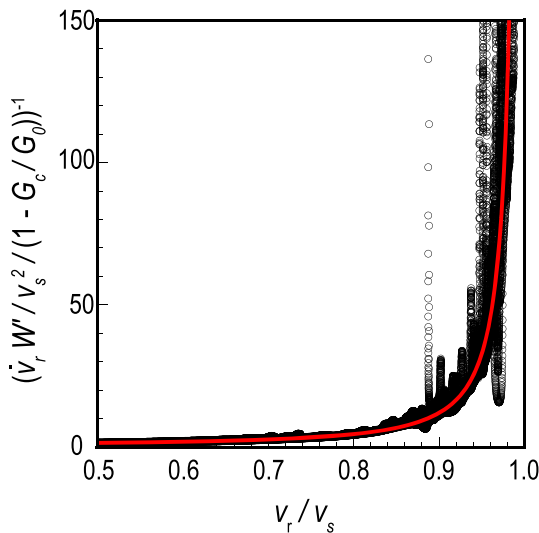


Figure 5. Inverse of normalized rupture acceleration (black circles) as a function of normalized rupture speed for the same models shown in Figure 4, compared with the theoretical estimation.

The right-hand side is a universal function that relates rupture speed to relative propagation length for a constant G_c/G_0 . After normalizing the

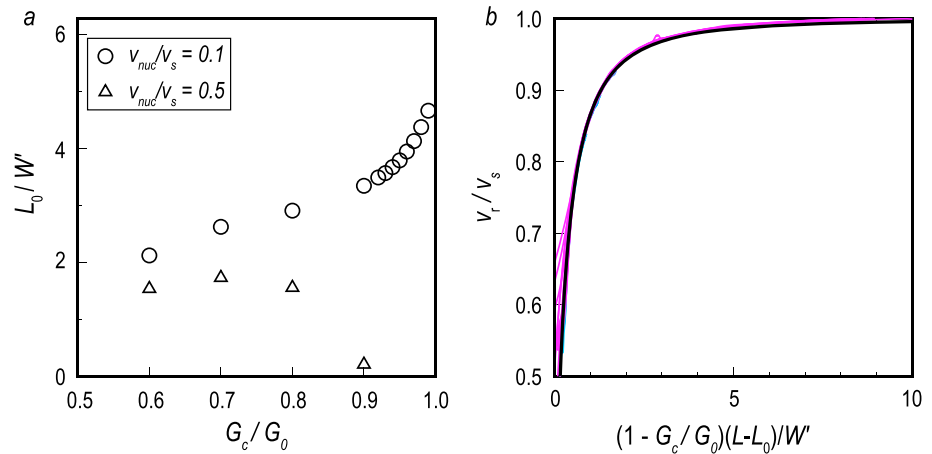


Figure 6. (a) The intercept of each predicted speed curve (e.g., in Figure 4a) with the horizontal axis as a function of G_c/G_0 . v_{nuc} is the nucleation speed of time weakening. (b) Normalized rupture speed as a function of normalized distance, compared with the theoretical estimation.

relative propagation length $L - L_0$ by $W'/(1 - G_c/G_0)$, all the rupture speed versus propagation length curves collapse onto this universal function (Figure 6b).

3.3. Effect of Steps in Fracture Energy and Stress Drop on Rupture Speed

As a first approximation to natural fault heterogeneity, we consider piecewise constant spatial distributions of fracture energy or stress drop along the fault. We design models with a step function in the spatial distribution of G_c , still such that $G_c/G_0 < 1$. We consider jumps of the ratio G_c/G_0 among the values 0.9, 0.96, and 0.98. We find that when ruptures run through an energy jump, their acceleration versus speed curves transition from one predicted curve to another one, both based on equation (15), after short transient adjustments (Figure 7).

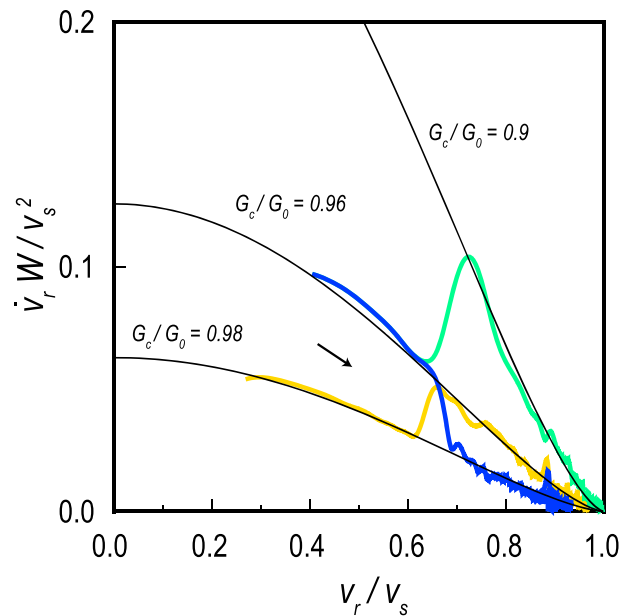


Figure 7. Rupture acceleration versus rupture speed (color curves) for the models with G_c/G_0 abruptly changing among 0.9, 0.96, and 0.98. The yellow, blue, and green curves result from simulations with jumps from 0.98 to 0.96, from 0.96 to 0.98, and from 0.96 to 0.9, respectively. The three black curves are the theoretical estimations of models with uniform $G_c/G_0 = 0.9, 0.96,$ and 0.98 , respectively. The arrow shows the direction of the evolution during the acceleration phase.

The results are similar for models with jumps in stress drop, especially at high rupture speeds. The steady energy release rate is proportional to the square of the stress intensity factor $K_{III}(v_r)$, which in turn is related to stress drop. A heterogeneous stress drop $\Delta\tau(x)$ contributes to K_{III} via a weighting function that decays sharply over a distance $\sim W' \alpha_s$ to the rupture tip (equation (55) in Appendix). As the rupture speed increases, α_s decreases, the weighting function decay becomes sharper (its decay length scale becomes much shorter than W'), and G_0 is increasingly controlled by the local value of $\Delta\tau(x)$. Thus, fast ruptures react rapidly to local changes in stress drop, over propagation distances shorter than W' .

3.4. Rupture Deceleration Phase in 2.5D

We now consider ruptures propagating into a region where $G_c/G_0 > 1$, such as a fault barrier with high fracture energy. When ruptures enter a barrier, they suffer a transient perturbation over a short propagation distance, then decelerate continuously, and eventually stop (Figures 8a and 8b). The deceleration rate depends on the energy ratio G_c/G_0 and on the rupture speed achieved before the rupture encounters the barrier. For smaller G_c/G_0 and higher starting speed, ruptures propagate a longer distance. We normalize the rupture deceleration, \dot{v}_r , by $v_s^2(1-G_c/G_0)/W'$ and find that all the rupture deceleration versus speed curves collapse onto another universal function of the form given by equation (14) (Figure 8c). We find that $A \approx 1.2$ and $P \approx 2.6$ are the best fitting values in the least squares sense, discarding the data within a short distance of the barriers. The deceleration phase is thus well described by the equation

$$\frac{\dot{v}_r W'}{v_s^2(1-G_c/G_0)} = 1.2\alpha_s^{2.6} \quad (20)$$

The normalized deceleration reaches a constant value 1.2 as the rupture speed drops to 0. This equation is very similar to that of the acceleration phase (equation (15)), but note that in equation (20) the signs of both \dot{v}_r and $1 - G_c/G_0$ are negative.

3.5. Rupture Arrest Distance Inside a Uniform Barrier

As in section 3.2, we obtain the following relation between rupture speed and propagation distance during deceleration, assuming constant G_c/G_0 in the fault barrier:

$$0.72 \left(\frac{G_c}{G_0} - 1 \right) (L_2 - L_1) / W' = \alpha_{s1}^{-0.6} - \alpha_{s2}^{-0.6} \quad (21)$$

With a suitable choice of reference position L_1 , this equation matches well the numerical results (Figures 8a and 8b). Setting L_2 such that $v_r = 0$, the length $L_{dece} = L_2 - L_1$ is the rupture arrest distance, that is, the maximum distance the rupture penetrates into the barrier. It is related to the peak rupture speed achieved before hitting the barrier by

$$L_{dece} = \frac{\alpha_s^{-0.6} - 1}{0.72(G_{cd}/G_{0d} - 1)} W' \quad (22)$$

where G_{cd}/G_{0a} is the energy ratio in the deceleration portion of the rupture. The value of α_s corresponding to the peak rupture speed is estimated from equation (18) as

$$\alpha_s = ((1 - G_{ca}/G_{0a}) L_{acce} / W' + 1)^{-1} \quad (23)$$

where L_{acce} and G_{ca}/G_{0a} are the rupture propagation distance and the energy ratio in the acceleration portion of the rupture. Substituting equation (23) into equation (22), we obtain the theoretical deceleration length L_{dece} and the total rupture length $L_{max} = L_{acce} + L_{dece}$. The simulated rupture lengths are compared with the theoretical estimations in Figure 9. Due to the oscillation of rupture speed immediately after the rupture encounters the barrier, which is not accounted for in our estimate, the theoretical L_{max} (equation (22)) slightly underestimates the simulated rupture length. If we approximately use $1.2\alpha_s^3$ instead of $1.2\alpha_s^{2.6}$ in the deceleration equation (20), we obtain a simpler relation that fits better the simulated deceleration length (Figure 9):

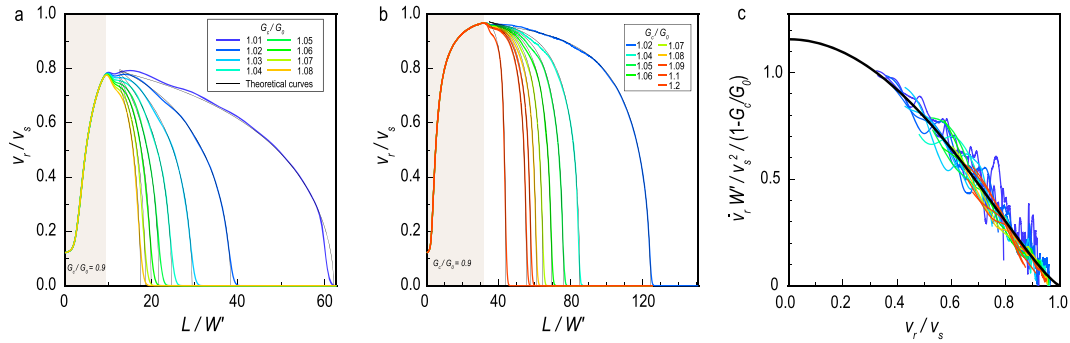


Figure 8. (a and b) Normalized rupture speed as a function of normalized distance from the 2.5-D numerical simulations for the models with $G_c/G_0 = 0.9$ in the gray regions and $G_c/G_0 > 1$ elsewhere. Models with different $G_c/G_0 (>1)$ are shown in different colors. (c) Normalized rupture deceleration as a function of normalized rupture speed, compared with the theoretical estimation.

$$L_{dece} \approx 0.83 \frac{(1-G_{ca}/G_{0a})}{(G_{ca}/G_{0d}-1)} L_{acce} \quad (24)$$

3.6. Rupture Through an Alternation of Asperities and Barriers

We next consider an alternation of asperities and barriers along the fault, that is, regions with $G_c/G_0 < 1$ and $G_c/G_0 > 1$, respectively (Figure 10a). The rupture speed accelerates inside the asperities and decelerates inside the barriers, in a regular cyclic pattern. When the rupture propagates from an asperity to a barrier, the rupture path in v_r-v_r' space jumps from the theoretical acceleration phase curve onto the deceleration phase curve, and vice versa, forming a closed loop (Figure 10b). These results illustrate how well the rupture-tip-equations-of-motion (equation (14)) describe the evolution of rupture speed for both acceleration and deceleration phases.

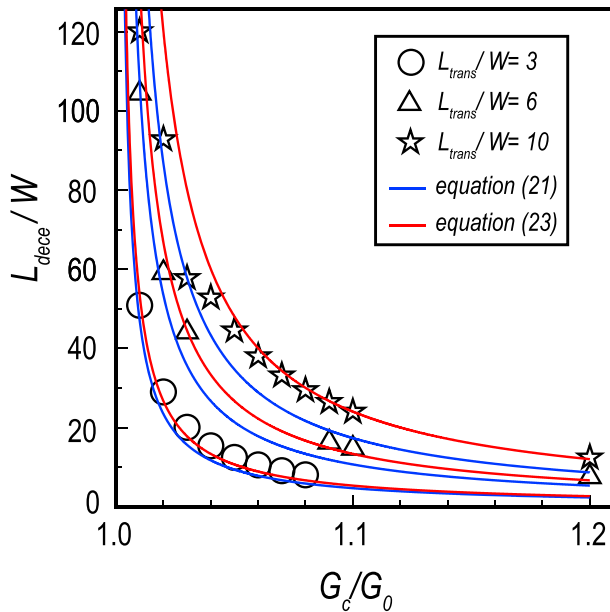


Figure 9. The normalized rupture length from 2.5-D simulations are shown as symbols for the model with G_c/G_0 changing abruptly from 0.9 to values larger than 1 at different transition distance L_{trans} . The blue curves are the theoretical estimations of rupture lengths based on equation (22) and the red curve is based on equation (24).

3.7. Results of 3-D Simulations Explained by 2.5-D Theory

We conducted a set of 3-D dynamic rupture simulations prescribing various values of the energy ratio G_c/G_0 , uniformly along the fault. To evaluate the along-strike rupture speed, we first calculate the rupture speed everywhere on the fault based on the gradient of rupture time, and then average it along depth at each along-strike position L . When $L/W > 2$, the along-dip component of the gradient of rupture time is negligible. We calculate the rupture acceleration as the time derivative of the depth-averaged rupture speed.

We find that the relation between rupture speed and propagation distance (Figure 11) in the 3-D model is well fitted by the 2.5-D equation (equation (18)). The only adjustment we find necessary is that the steady energy release rate in 3D is slightly smaller than in 2.5D:

$$G_0 = \frac{0.96 \Delta \tau^2 W}{\pi \mu} \quad (25)$$

which implies $\gamma = 0.96/\pi$. In our 2.5-D numerical model $\gamma = 1/\pi$ comes from a half-wavelength proxy for the depth profile of slip. Lehner et al. (1981) chose a different value, $\gamma = \pi/8$, for a full-space model ($\gamma = \pi/4$ for a half-space model) based on the criterion that the slip of an infinitely long crack with uniform stress drop should match in the 2.5-D and 3-D models. Our results indicate that the 2.5-D model with $\gamma = 1/\pi$ is a very good approximation of the 3-D model.

To investigate the deceleration phase in the 3-D model, we set $G_c/G_0 > 1$ and a fast nucleation speed, $0.8 v_s$, inside the nucleation zone $L/W < 2$.

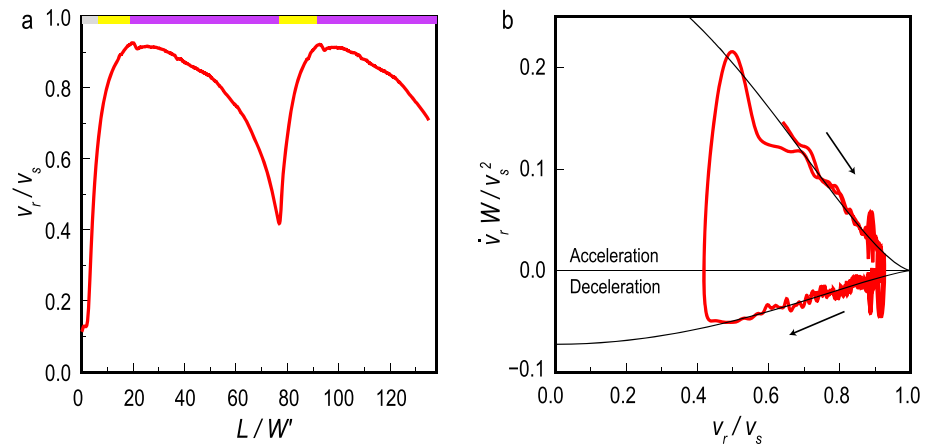


Figure 10. (a) Rupture speed evolution for the model with G_c/G_0 abruptly changing between 0.9 (yellow bars) and 1.02 (purple bars). The gray bar indicates the nucleation zone. (b) Rupture acceleration versus rupture speed for the same model. The arrows show the direction of the evolution between acceleration and deceleration phases.

Outside the nucleation zone, the ruptures decelerate. The relation between rupture speed and propagation distance in 3D (Figure 12) is fitted well by the 2.5-D deceleration rupture-tip-equation-of-motion (equation (21)).

4. Discussion

4.1. Scope of the LEFM Assumption

Our theoretical analysis is based on LEFM and should be adequate when the ratio Λ_0/W' of static cohesive zone size (defined in equation (13)) to reduced rupture width is small. The simulation results and theoretical predictions agree well if $\Lambda_0/W' \leq 1$ (Figure 13). For smaller Λ_0/W' , such as 0.314, 0.157, and 0.1, we run models with $G_c/G_0 = 0.9$ and find the resulting rupture speed distributions converge to the LEFM prediction. The condition of the rupture-tip-equation-of-motion for elongated ruptures is $\Lambda_0/W' \leq 1$.

4.2. Effects of Finite Seismogenic Depth

The approximate rupture-tip-equation-of-motion proposed here for ruptures on bounded faults in 2.5D and 3D is the same as that of a crack in a bounded strip in 2D (Goldman et al., 2010) after minor adjustments (replacing the term $v_s^2 \alpha_s^3$ by $2v_p^2 \alpha_R^4$). The definition of width W is different in these two situations: in the strip configuration W is the thickness of the elastic medium in the crack-normal direction, whereas in the 2.5-D and 3-D models it is the width of the rupture area in the dimension perpendicular to the rupture propagation direction. Despite this difference, the steady energy release rate shares the same form, $G_0 = \gamma \Delta \tau^2 W / \mu$, where γ is a different geometric factor for each configuration. The property of constant energy release rate (independent of rupture length) is one feature distinguishing elongated rupture models from other usual rupture models such as the circular crack in 3D and the linear crack in 2D.

Our theoretical developments highlight the essential role of the seismogenic width on rupture dynamics. The finiteness of the seismogenic width has, in theory, important effects on numerous other aspects of earthquake rupture. It affects earthquake moment versus area scaling relations by limiting the elastic stiffness of a slip zone (Luo et al., 2017). Fracture mechanics theory and dynamic rupture simulations indicate that the seismogenic width controls the maximum fault-step over distance that a rupture can jump (Bai & Ampuero, 2017) and the maximum thickness of fault damage zones (Ampuero & Mao, 2017). It has also been

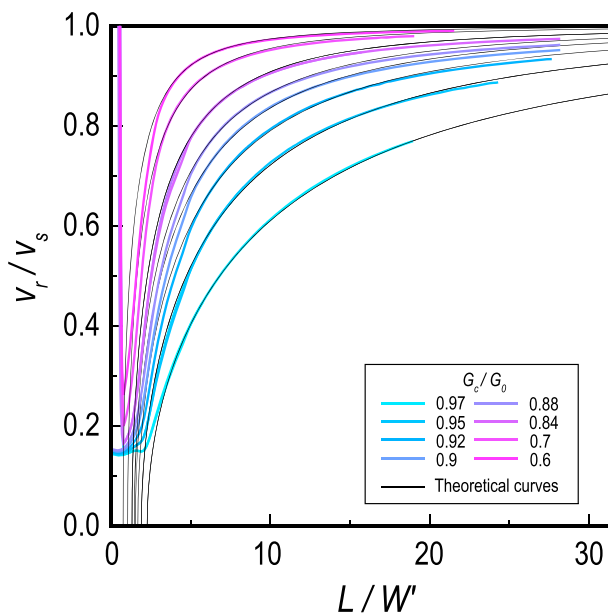


Figure 11. Normalized rupture speed (colored curves coded by $G_c/G_0 < 1$) as a function of normalized distance from the 3-D numerical models versus theoretical estimation (black thin curves).

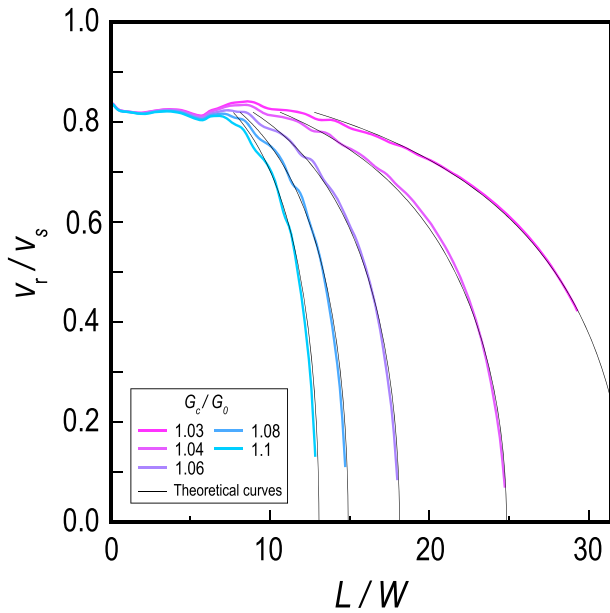


Figure 12. Normalized rupture speed (colored curves coded by $G_c/G_0 > 1$) as a function of normalized distance from the 3-D numerical models versus theoretical estimation (black thin curves).

proposed that continental strike-slip earthquakes have a characteristic length of segmentation related to the seismogenic width (Klinger, 2010), a feature found in 3-D earthquake models (Heimpel, 2003). Our results can also help anticipate the range of rupture scenarios possible in faults where the seismogenic width changes substantially along strike, that is, the San Andreas Fault (Smith-Konter et al., 2011) and the Alpine Fault in New Zealand (Michailos et al., 2019).

The finiteness of the seismogenic width is an essential ingredient of natural faults that has been rarely accounted for in laboratory experiments of dynamic rupture. A notable exception is the experimental work by (Mello et al., 2014), who considered a frictional interface partitioned in two elongated bands of different roughness, a rough (seismogenic) portion obtained by bead blasting, and a smooth (aseismic) portion obtained by polishing. Based on our theoretical results, new targets for such laboratory experiments can be designed, for instance on surfaces with controlled heterogeneities along strike, to probe 3-D earthquake mechanics at a fundamental level.

4.3. Stability of Steady State Ruptures

4.3.1. Constant Fracture Energy

If fracture energy G_c is constant, the rupture-tip-equation-of-motion predicts rupture acceleration toward the S wave speed. However, the equation also admits steady ruptures at speeds arbitrarily slower than v_s

if G_c is exactly equal to the steady energy release rate G_0 . In numerical simulations, these slow steady solutions can be approached by artificial initial conditions, but they are unstable. While the equation does not constrain their speed, it provides insight on their stability to perturbations. To simplify the analysis,

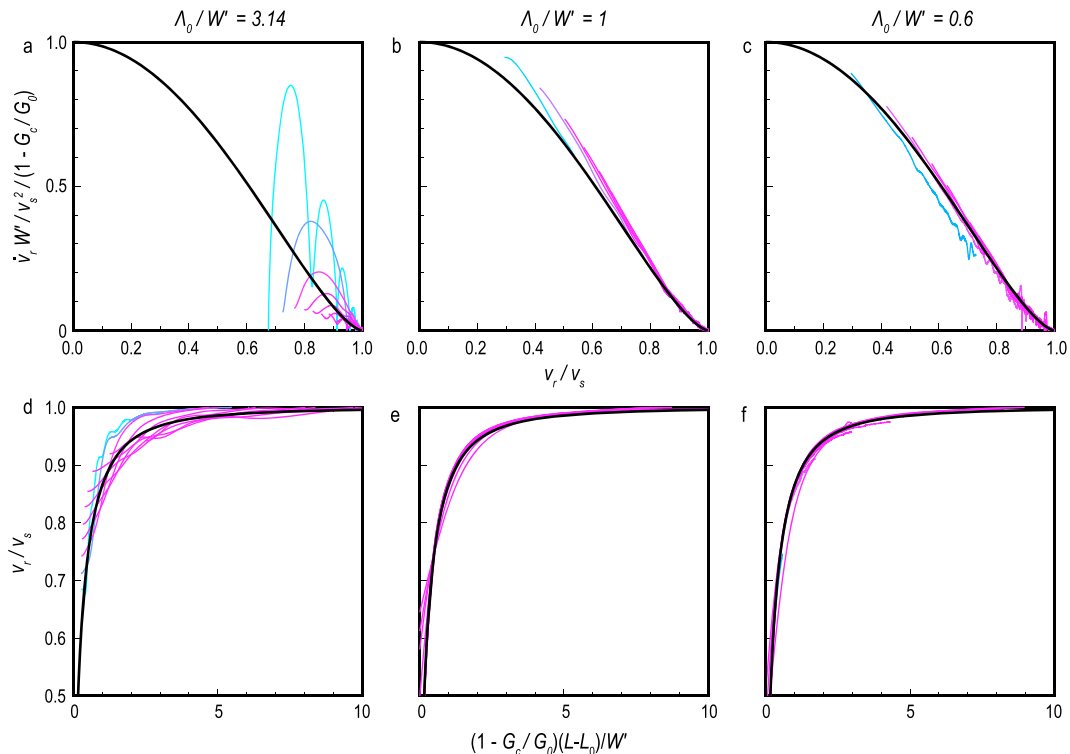


Figure 13. (a–c) Normalized rupture acceleration as a function of normalized rupture speed for different ratio Λ_0/W' , compared with the theoretical estimation. (d and e) Normalized rupture speed as a function of normalized distance for different ratio Λ_0/W' , compared with the theoretical estimation.

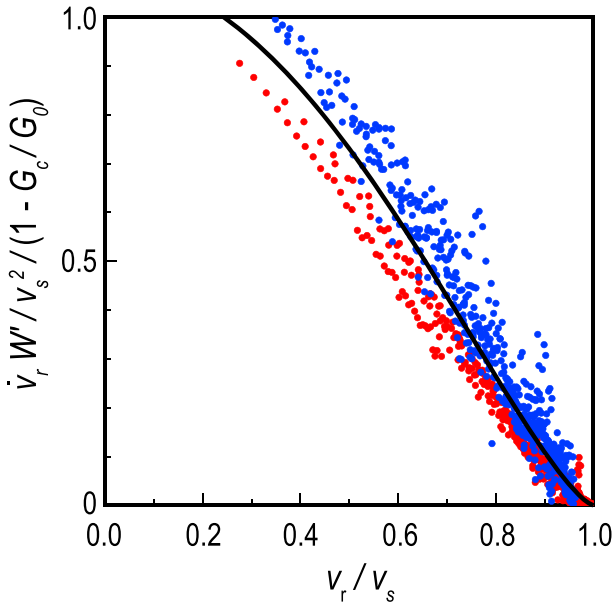


Figure 14. Normalized rupture acceleration (red dots) and deceleration (blue dots) as a function of normalized rupture speed compared with a unique best fit curve.

we use a single equation for both the acceleration and deceleration phases, obtained by fitting their data together (Figure 14):

$$\frac{\dot{v}_r W'}{v_s^2 (1 - G_c / G_0)} = \alpha_s^{2.6} \quad (26)$$

Normalizing the rupture speed and distance, that is, $\tilde{v} = v_r / v_s$ and $\tilde{L} = L / W'$, equation (26) can be written as

$$\frac{d\tilde{v}}{\tilde{v}} = \frac{\alpha_s^{2.6}}{\tilde{v}^2} (1 - G_c / G_0) d\tilde{L} \quad (27)$$

If a steady state rupture with $G_c / G_0 = 1$ encounters a perturbation of fracture energy ΔG_c , its rupture speed is perturbed according to

$$\frac{d\tilde{v}}{\tilde{v}} = \frac{(1 - \tilde{v}^2)^{1.3}}{\tilde{v}^2} \frac{\Delta G_c}{G_0} d\tilde{L} \quad (28)$$

The rupture speed diverges from its initial steady state value: it accelerates (decelerates) if ΔG_c is positive (negative). The maximum disturbance ΔG_c that causes a relative perturbation of rupture speed of less than 10%, that is, $d\tilde{v} / \tilde{v} < 10\%$, at a propagation distance $d\tilde{L} = 10$ is estimated from equation (28) as $\frac{\Delta G_c}{G_0} = 0.01 \tilde{v}^2 / (1 - \tilde{v}^2)^{1.3}$. The maximum allowed

disturbance increases with increasing rupture speed; thus, fast ruptures are more stable than slow ruptures. For instance, for a rupture speed $\tilde{v} = 0.9$ the maximum allowed disturbance is about 7%, and for $\tilde{v} = 0.1$ it is about 0.01%. This analysis, under the assumption of a constant G_c , implies that for a slow steady rupture to be stable additional mechanisms are required. One such mechanism is conceptually explored next.

4.3.2. Speed-Dependent Fracture Energy

If fracture energy depends on rupture speed, the speed of steady ruptures is well determined by the condition $G_c(v_r) = G_0$. This condition results in steady speeds that can be lower than the limiting speed (S wave speed in mode III). The stability of such steady state ruptures depends on the sign of dG_c / dv_r . If the fracture energy increases with increasing rupture speed (“speed strengthening”), then the steady state rupture speed is stable: if a perturbation acting on a steady state rupture induces a small increase of rupture speed Δv_r , the energy ratio increases and becomes $G_c(v_r + \Delta v_r) / G_0 > 1$. Then, according to equation (15) or equation (20), rupture decelerates counteracting the perturbation. Thus, speed strengthening provides a negative feedback that stabilizes steady state ruptures. In contrast, if the fracture energy decreases with increasing rupture speed (“speed weakening”), ruptures rapidly accelerate to the S wave speed, as described by the rupture-tip-equation-of-motion.

If speed-strengthening effects operate on natural faults, stable steady state ruptures significantly slower than the limiting speeds may exist once G_0 is balanced by $G_c(v_r)$. A speed dependence of G_c can emerge indirectly from an explicit dependence of friction on slip velocity, as in rate-and-state-dependent friction (Ampuero & Ben-Zion, 2008; Ampuero & Rubin, 2008; Rubin & Ampuero, 2005), in combination with the systematic relation between rupture speed and peak slip velocity (Gabriel et al., 2013). Laboratory experiments on analog materials indeed show that fracture energy increases with rupture speed (Goldman et al., 2010). Off-fault inelasticity (plasticity or damage) can also increase the total dissipated energy G_c by an amount that depends on rupture speed due to the speed dependence of the thickness H of the inelastic zone (Gabriel et al., 2013). The latter scales with K_{III}^2 (e.g., Ampuero & Mao, 2017) which, from equation (9) for large ruptures ($L \gg W$), is proportional to $\alpha_s W$. Because the function α_s decreases with rupture speed, if the overall G_c is proportional to H (for instance, if the off-fault dissipated energy per unit of volume is constant, rate-independent), the implied behavior is speed weakening, for which the only steady state speed predicted by the model is v_s . A rate-dependent rheology (on- or off-fault) seems necessary to produce the speed strengthening $G_c(v_r)$ required for stable steady rupture at low speed.

4.4. High-Frequency Radiation

We rewrite the rupture-tip-equation-of-motion (equation (15)) as

$$\frac{d\tilde{v}/v_s}{\alpha_s^3} = d\tilde{t} \quad (29)$$

where \tilde{v} is the normalized speed, $\tilde{v} = v_r/v_s$, and \tilde{t} is the normalized time, $\tilde{t} = v_s t(1-G_c/G_0)/W'$. Integrating equation (29) for \tilde{v} from 0 to \tilde{v} and for \tilde{t} from 0 to \tilde{t} , assuming constant G_c/G_0 , we obtain a simple relation between rupture speed and time:

$$\tilde{v} = \frac{\tilde{t}}{\sqrt{1+\tilde{t}^2}} \quad (30)$$

Multiplying both sides by dt and integrating with respect to time, we get

$$(1-G_c/G_0)L/W' + 1 = \sqrt{1+\tilde{t}^2} \quad (31)$$

At the beginning of rupture, when $\tilde{t} \ll 1$, the rupture speed increases linearly with time, $\tilde{v} \approx \tilde{t}$. Note that this is a rupture speed averaged across the seismogenic width, and the smaller-scale nucleation process is ignored. As time increases, such that $\tilde{t} \gg 1$, rupture speed asymptotically approaches 1. Equations (30) and (31) can be applied to the rupture deceleration by replacing \tilde{t} with $\tilde{t}_{total} - \tilde{t}$, where \tilde{t}_{total} is the total rupture time. The dimensionalized form for the beginning and stopping stages of rupture are, respectively,

$$v_r \approx \frac{v_s^2 t}{W'} \left(1 - \frac{G_c}{G_0}\right) \text{ and } v_r \approx \frac{v_s^2 (t_{total} - t)}{W'} \left(1 - \frac{G_c}{G_0}\right) \quad (32)$$

Equation (32) features slope discontinuities at the onset and end of rupture, whose amplitude is proportional to $(1 - G_c/G_0)$. Raul Madariaga (1977) found that suddenly starting and stopping cracks create discontinuities in the radiated wavefield that enhance its high-frequency content. Although less abruptly, the starting and stopping phases along elongated faults also contribute to the radiated high-frequency energy.

A fundamental feature of the 2.5-D and 3-D rupture-tip-equations-of-motion is the implication that long ruptures have inertia, which introduces a memory effect. When the rupture encounters an abrupt change of fracture energy, its speed does not change instantaneously, but reacts with a continuous transient (Figures 8a, 8b, and 10). In contrast, in 2-D crack models rupture speed reacts immediately to abrupt changes of fracture energy (Raul Madariaga, 1983). Thus, the relations between wave radiation and fault heterogeneity are different in 2-D and in elongated 3-D ruptures. Another notable difference is that $G_0 - G_c$ is a radiated energy density in 2D (e.g., Madariaga et al., 2006), but not in 3D. In fact, according to the 3-D rupture-tip-equation-of-motion, $G_0 - G_c$ has the same sign as rupture acceleration, \dot{v}_r , but both acceleration and deceleration phases are expected to make positive contributions to radiated energy.

4.5. The Rupture Potential of Faults

4.5.1. Definition of Rupture Potential

We consider a fault with a spatially heterogeneous (along-strike) distribution of energy ratio G_c/G_0 . Unlike in section 3.6, where we considered piecewise constant heterogeneities, here we consider arbitrary heterogeneities. Note that G_c and G_0 are averaged along depth. Whether a rupture front stops is determined by the rupture-tip-equation-of-motion. Using the same exponent P in both acceleration and deceleration phases, as in section 4.3.1, we rewrite the rupture-tip-equation-of-motion as

$$\frac{v_r dv_r}{v_s^2 \alpha_s^P} = A(1-G_c/G_0) dx/W' \quad (33)$$

where $dx = v_r dt$, $A = 1$ if $G_c/G_0 < 1$, and $A = 1.2$ if $G_c/G_0 > 1$. Integrating this equation along strike, we obtain

$$\frac{1}{P-2} (\alpha_s^{2-P} - 1) \Big|_{v_{r1}}^{v_{r2}} = \int_{L_1}^{L_2} A(1 - G_c/G_0) dx/W' \quad (34)$$

where $\alpha_s^{2-P} - 1$ ($P \approx 2.6$) increases from 0 to ∞ as rupture speed increases from 0 to v_s , v_{r1} and v_{r2} are the initial and final rupture speeds, and L_1 and L_2 are the initial and final rupture locations along the fault. We define the “rupture potential” $\varphi(L)$ as

$$\varphi(L) = \int_0^L A(1 - G_c/G_0) dx/W' \quad (35)$$

where 0 is an arbitrary reference location on the fault and L is the relative location (the positive and negative directions along strike can be chosen arbitrarily). The right side of the equation (34) is the rupture potential change over a specific portion of fault (L_1, L_2) and can be rewritten as

$$\Phi(L_1, L_2) = \varphi(L_2) - \varphi(L_1) \quad (36)$$

where rupture propagates from L_1 to L_2 ($L_1 < L_2$). For a rupture front propagating in the opposite direction, from L_2 to L_1 , the rupture potential change is $\Phi(L_2, L_1) = -\Phi(L_1, L_2)$. Note that the rupture potential defined here for long ruptures in 3D is fundamentally different than the one proposed by Kaneko et al. (2010) based on a 2-D problem and on 3-D simulations of ruptures with small aspect ratio.

The rupture potential $\varphi(x)$ is variable during interseismic periods. Tectonic loading increases shear stresses, thus $\Delta\tau$ and G_0 , along the fault. Observations indicate that fracture energy is not constant, and theoretical models of fault weakening imply a slip dependency in the form $G_c \propto D^n$ (e.g., Viesca & Garagash, 2015), where D is the final slip. For very long ruptures $D \propto W\Delta\tau/\mu$, thus $G_c \propto \Delta\tau^n$ and $G_c/G_0 \propto \Delta\tau^{n-2}$. For thermal pressurization $n = 2/3$ (Viesca & Garagash, 2015) and for off-fault inelastic dissipation $n = 1$ (Andrews, 2005; Gabriel et al., 2013). In both cases, $n - 2 < 0$ and G_c/G_0 decreases with increasing load (increasing $\Delta\tau$). The rupture potential of a fault is thus an increasing function of time $\varphi(x, t)$. Since the stressing rate of barriers ($G_c/G_0 > 1$) and asperities ($G_c/G_0 < 1$) may be different during interseismic periods (Kaneko et al., 2010), we consider two end-member cases: a “low-stressing-barrier model” in which barriers are creeping and have zero stressing rate (Figure 15a) and a “high-stressing-barrier model” in which barriers have the same stressing rate as asperities (Figure 15b). In the latter case, the barriers shrink and the asperities expand as stress loading increases; thus, the rupture potential of asperities increases faster than in the former case.

In addition to the rupture potential, we also define a “rupture kinetics” term E based on the left-hand side of equation (34) as

$$E(v_r/v_s) = \frac{1}{P-2} (\alpha_s^{2-P} - 1) \quad (37)$$

E increases from 0 to infinity as v_r increases from 0 to the limiting speed v_s . The left side of equation (34) is the rupture kinetics change, $\Delta E = E(v_{r2}/v_s) - E(v_{r1}/v_s)$, over a specific portion of fault rupture (L_1, L_2). Conceptually, equation (34) represents energy conversion between potential energy and kinetic energy, although both the rupture potential and rupture kinetics are defined as nondimensional quantities.

4.5.2. Determining the Size of the Next Earthquake by the Rupture Potential

Assuming $v_{r1} = 0$ at the rupture onset and considering $v_{r2} = 0$ when the rupture stops, the left side of equation (34) becomes 0 at the end of a rupture. The condition for rupture arrest is thus $\varphi(L_2) = \varphi(L_1)$. For a given nucleation location L_1 , this condition may be satisfied at multiple locations L_2 . The one closest to L_1 is the final rupture arrest location: the rupture stops at the first opportunity. The same arrest criterion applies to both rupture fronts of a bilateral rupture that starts at location L_0 : it stops at the nearest locations L_- and L_+ such that $\varphi(L_0) = \varphi(L_-) = \varphi(L_+)$.

In theory, this arrest criterion can be used to determine the potential size of the next earthquake provided that the spatial distribution of G_c/G_0 is known. The graphical application of the arrest criterion is illustrated for the two end-member barrier models in Figure 15. Note that the final rupture tip positions depend on the nucleation location. The potential earthquake size increases with time continuously (e.g., location A in Figure 15), except for abrupt jumps that occur when $\varphi(L_-)$ or $\varphi(L_+)$ reach maxima or

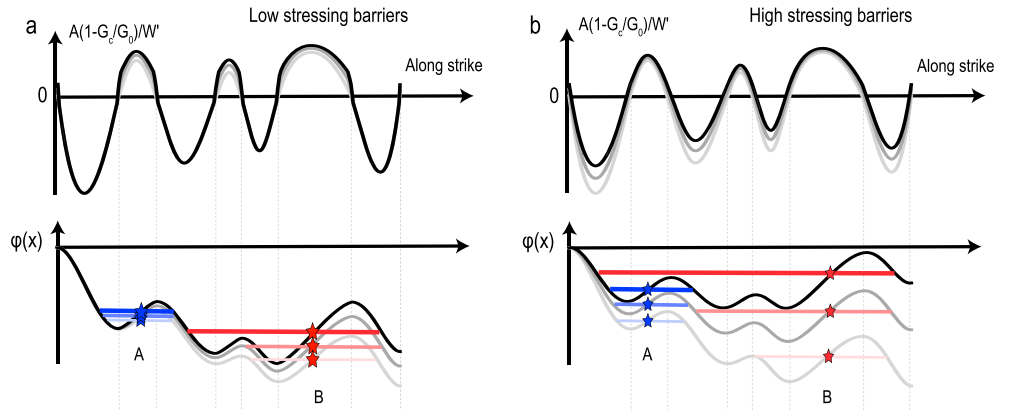


Figure 15. A conceptual model for determining earthquake size by the rupture potential. (top) The curves (time increases from light gray to black) show the along-strike distribution of $A(1 - G_c/G_0)/W$. (bottom) The curves (time increases from light gray to black) are the rupture potential $\varphi(x,t)$. The bars are examples of earthquake rupture zones, nucleated on the stars (locations A and B). For each rupture, the final rupture tips are determined as the nearest locations to the hypocenter at which the value of the rupture potential $\varphi(x)$ returns to the same value as at the hypocenter (nearest points of intersection between the black curve and a horizontal line). The stressing rate in barriers is very low (a). The stressing rate in barriers is same as in asperities (b).

minima of the rupture potential $\varphi(x)$ (e.g., location B in Figure 15). Such abrupt jumps of earthquake size may explain why some faults have hosted unexpectedly large earthquakes compared to their historic events (Ammon et al., 2005; Wang et al., 2011).

The potential size of the next earthquake can also be evaluated probabilistically as follows. The probability distribution $\rho(x)$ of nucleation at along-strike position x could be assumed uniformly random or informed by analysis of background seismicity or tectonic stressing rate (e.g., concentrated near the edges of creeping segments). For each possible hypocenter position x , one can deterministically evaluate the final rupture size $L(x) = L_+ - L_-$ by the above arrest conditions. Combining $\rho(x)$ and $L(x)$, the probability distribution of rupture sizes can be constructed. Thus, the model developed here provides a framework for physics-based probabilistic hazard assessment.

The foregoing model assumes that the rupture is continuous, uninterrupted along the fault. In particular, it does not consider ruptures that break fault segments that are separated by a finite distance. Recent advances have been made in the theoretical understanding of factors controlling multisegment ruptures, including rupture jumps across fault step overs (Bai & Ampuero, 2017). Integrating the present model with physics-based multisegment rupture criteria is an important objective for future work. In the next subsection we examine the more tractable problem of contiguous fault segments.

4.5.3. Multiple Rupture Cycles

The rupture potential also helps conceptualize fault behavior during a sequence of multiple ruptures and earthquake cycles. Here we consider a simple conceptual model of earthquake cycle, where a rectangular seismogenic portion of a fault is loaded by steady creep on both the deeper portion of the fault and on one side of the seismogenic segment (Figure 16). At the cycle onset, the stress along strike is at its residual strength, τ_d . We assume that the stressing rate has the following distribution along strike:

$$\dot{\tau}(L) = \gamma_l \exp(-L/W) + \gamma_b \quad (38)$$

where L is the distance to the lateral creeping boundary and the two terms are the contributions from the lateral and bottom creeping portions, respectively. We assume that earthquakes start at the boundary between the lateral creep portion and the seismogenic portion when the stress at $L = 0$ reaches the static fault strength τ_s .

The key of this model is to determine the rupture size of each earthquake. As discussed in the previous section, we can assume that $G_c/G_0 = B\Delta\tau^{n-2}$, where B is a constant and $\Delta\tau = \tau(L,t) - \tau_d$. For simplicity, we assume that $A = 1$ for both acceleration and deceleration phases; thus, $A(1 - G_c/G_0) = 1 - B\Delta\tau^{n-2}$.

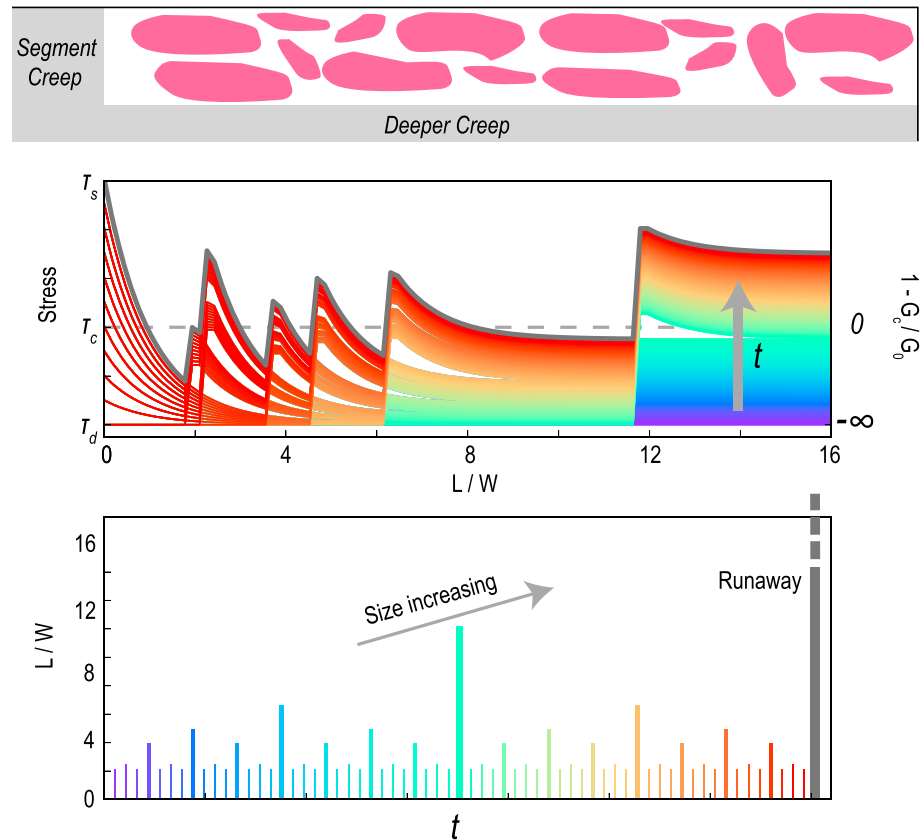


Figure 16. A conceptual model for earthquake supercycles. (top) A Rectangular seismogenic portion of a fault (pink areas) is surrounded by the deeper creeping portion of the fault and one side of the creeping segment (gray areas). (middle) The evolution of stress along strike, bounded between fault strength τ_s and residual stress τ_d , during one supercycle. The gray dashed line indicates the critical stress τ_c , at which $1 - G_c/G_0 = 0$ as shown at the right vertical axis. The colors of curves changing from purple to red denote the increasing loading time t (gray arrow). The thick gray curve shows the stress distribution before the runaway earthquake. (bottom) The earthquake sequences versus time. The colors of bars correspond to the colors in the middle figure. The gray bar marks the biggest earthquake (runaway) of a supercycle.

As $\Delta\tau$ increases from 0 to $\tau_s - \tau_d$, $A(1 - G_c/G_0)$ increases from $-\infty$ to $1 - B(\tau_s - \tau_d)^{n-2}$. We assume that $1 - B(\tau_s - \tau_d)^{n-2} > 0$ and define a critical stress τ_c between τ_d and τ_s such that $1 - B(\tau_c - \tau_d)^{n-2} = 0$. The rupture size is determined as discussed in section 4.5.2. At the end of each earthquake, the stress drops to τ_d in the rupture area ($L < L_{co}$) and increases in its neighboring area ($L > L_{co}$) as $\Delta\tau_{co} \exp(-(L - L_{co})/W)$, where $\Delta\tau_{co}$ is the coseismic stress drop. Then the interseismic stressing rate resumes according to equation (38) and the procedure is repeated until the next event.

Based on these assumptions, we can obtain the evolution of stress and earthquake sequences (Figure 16). The model leads to cycles composed of small and large events. Early in a cycle, the ruptures propagate short distances due to the low stress level of the entire fault. These small events occur regularly with an interval $T_{small} = (\tau_s - \tau_d)/\gamma_l$. As the loading by earthquakes and the continuous bottom loading accumulate, ruptures can propagate further and further. Eventually, once the average stress of the entire fault becomes higher than the critical stress τ_c a rupture can break through neighboring barriers and bridges multiple asperities along strike (gray curve in Figure 16). Such a runaway “superrupture” stops only when it reaches a strong barrier segment. The interval between superruptures is on the order of $T_{super} = (\tau_c - \tau_d)/\gamma_b$. This conceptual model helps rationalize one type of “supercycles” observed on segmented faults, in which single-segment ruptures occur in between large multisegment ruptures. We note that if instead $1 - B(\tau_s - \tau_d)^{n-2} < 0$, the seismogenic fault behaves as a barrier where all ruptures stop spontaneously (no runaway rupture).

4.5.4. Dependency of Self-Arrested Rupture Length on Seismogenic Width

In 3-D dynamic rupture simulations initiated by an overstressed nucleation area, on faults with uniform friction properties and initial stress, Weng and Yang (2017) found that ruptures with small enough width W were self-arrested (stopped spontaneously). Their final rupture length and aspect ratio increased as W was increased, until a critical W was reached that led to runaway ruptures (unstoppable on a homogeneous fault). Their results can be understood in the framework of our conceptual model as follows. The overstressed nucleation zone, of size L_{nuc} , constitutes an asperity with positive rupture potential $\Phi_a = \Phi(0, L_{nuc})$. The fault area where the rupture stops spontaneously must be a barrier with negative rupture potential $\Phi_b = \Phi(L_{nuc}, L)$. Considering the arrest condition $\Phi_a + \Phi_b = 0$, the final rupture length is $L = L_{nuc} + L_b$ with $L_b/W = \gamma\Phi_a/A(G_c/G_0 - 1)$, where G_c and G_0 are constant. The coefficient A may be different than 1.2 for in-plane rupture. Because $G_0 \propto W$, as W increases, L_b/W increases. At a critical width such that $G_c/G_0 = 1$, $L_b/W \rightarrow \infty$ and the self-arrested rupture length becomes infinite. The derived rupture aspect ratios as a function of rupture width (blue curves in Figure 2b) are consistent with the results of 3-D dynamic rupture simulations by Weng and Yang (2017) (gray curves in Figure 2b). At larger widths, Φ_b is positive, the barrier becomes an asperity, and the rupture is runaway. Interestingly, the largest self-arrested rupture length is infinite, which is in contrast with the finite maximum self-arrested rupture size found in 3-D problems without confined seismogenic depth (Galis et al., 2017; Galis et al., 2018).

4.5.5. Constraints on Rupture Potential

In order to evaluate the rupture potential of natural fault segments, an estimate of the energy ratio $G_c/G_0 = G_c\mu/\gamma\Delta\tau^2W$ along the fault is needed. Some of the quantities involved currently have large uncertainties. The shear modulus μ in the crust is well known at the large scales of interest. The seismogenic width W is usually constrained by the geodetic locking depth, by the depth distribution of background seismicity, or by thermal modeling. Geodetic observations, including GPS, InSAR, and leveling data, can provide estimates of long-term slip deficit and its spatial distribution, from which tectonic stressing rates can be derived (e.g. Ader et al., 2012; Karimzadeh et al., 2013; Metois et al., 2012). The stress drop $\Delta\tau$ may be constrained by such stress modeling. To first order, it is related to the depth-averaged slip deficit D by the following elasticity relation on a seismogenic zone of finite width: $\Delta\tau = C\mu D/W$, where C is a geometric factor of order 1 (Kanamori & Anderson, 1975). The fracture energy G_c may be constrained by scaling relations or physical models (Rice, 2006; Viesca & Garagash, 2015), but remains the most uncertain parameter in the equation. The present model thus sheds light on the challenges and opportunities in the development of physics-based earthquake hazard methods.

4.5.6. Rupture Through Creeping Fault Segments

An interesting question that can be addressed in the framework of this theory is as follows: can an earthquake rupture break through a creeping fault segment? Many large faults have segments that creep steadily and are thought to behave as rupture barriers (Harris, 2017), for instance the San Andreas fault creeping segment in central California, the Peruvian subduction zone on the Nazca ridge (Perfettini et al., 2010), and the Arauco and Mejillones intersegments on the central Chile subduction zone (Metois et al., 2012). Creep prevents stress build up, which tends to limit the potential stress drop, leading to low G_0 and low rupture potential of the creeping barrier. However, thermal weakening can occur in the creeping segment as the earthquake rupture penetrates and induces high slip rates (Noda & Lapusta, 2013). In an extreme scenario, this results in total reduction of frictional strength. The resulting stress drop in the creeping barrier is equal to the effective normal stress times the (low) friction coefficient at the background creep rate, and can be comparable to the typical stress drop of an earthquake (a few megapascals), which increases the rupture potential of the barrier and may even turn it into an asperity (positive potential). Thus, earthquake rupture through a creeping fault segment cannot be ruled out on the physical grounds of the present model.

4.6. Interpretation of Fluctuations of Rupture Speed

The rupture-tip-equation-of-motion provides a useful framework to interpret the fluctuations of rupture speed and final slip observed along earthquake ruptures in terms of fluctuations of the energy ratio G_c/G_0 . We take as an example the 2004 Sumatra-Andaman earthquake. The propagation along strike of this megathrust event can be described by three main segments (Ammon et al., 2005). In the initial segment, the rupture speed was slow and slip was low, which corresponds to G_c/G_0 slightly smaller than 1. In the

middle segment, rupture speed was high and final slip was large, which implies that G_c/G_0 is significantly smaller than 1. In the last segment, the final slip decreased, which implies that G_c/G_0 increases, but it is not clear whether it exceeded 1. If $G_c/G_0 > 1$, the rupture decelerated progressively and we could estimate G_c/G_0 based on the length of this segment. But if $G_c/G_0 < 1$ the rupture in this segment may have accelerated until it was finally stopped by a strong barrier.

4.7. Implications for Source Inversion

For very large earthquakes whose rupture length exceeds the rupture width, average rupture speeds can be estimated from seismological data (Ammon et al., 2005; Ishii et al., 2005). However, lateral variations of rupture speed are usually difficult to obtain due to the trade-off with other parameters in the slip inversion (Wei et al., 2013), although backprojection rupture imaging can provide further constraints (e.g., Bao et al., 2019, Wang et al., 2016). The model developed here reveals relations between kinematic source properties and dynamic fault properties: equation (27) shows that the rupture speed gradient, dv_r/dL , is proportional to the fault parameter $(1 - G_c/G_0)$. This suggests to use the rupture-tip-equation-of-motion derived here as a physics-based constraint in slip inversions in order to reduce trade-offs. However, it is not obvious that trade-offs can be strongly reduced, because the new equation also involves an additional unknown, G_c . Progress can be done by adopting as prior a theoretical or empirical relation between fracture energy G_c and final slip, like those proposed by Viesca and Garagash (2015).

4.8. Implications for Source Time Functions

Source time functions (STF) can be obtained robustly from earthquake data (e.g., Vallée et al., 2011). The moment function of a fault with constant seismogenic width W is $M_0(t) = \mu W \int_0^{L(t)} D(x) dx$ and static elasticity dictates $D(x) = W \Delta \tau(x) / C \mu$, where $\Delta \tau(x)$ and $D(x)$ are the depth-averaged stress drop and final slip and C is a geometric factor of order 1. Then the STF has the form

$$\dot{M}_0(t) = W^2 \Delta \tau v_r / C \quad (39)$$

Combining this moment-rate equation with the rupture-tip-equation-of-motion, one can numerically solve for the rupture speed and stress drop distributions along strike based on the STF if an additional assumption is adopted, for instance, a relation between G_c and final slip. This approach could be used to infer statistical properties of fault stress and strength from the statistical properties of large catalogs of STFs (Meier et al., 2017). If the slip (and thus stress drop) distribution has been well constrained for an event, for instance by geodetic or remote sensing data, the rupture speed distribution can be computed from equation (39) and then the fracture energy distribution can be derived from the rupture-tip-equation-of-motion.

4.9. Implications for Radiated Energy

Nonsteady ruptures radiate far-field waves: both acceleration and deceleration phases make positive contributions to radiated energy. To examine implications for the radiated energy, E_r , of a depth-bounded rupture in 3D, we assume a special case with constant W and G_0 and rewrite equation (34) as

$$\int_{L_1}^{L_2} A(G_0 - G_c) W dx = \frac{W' W G_0}{P-2} (\alpha_s^{2-P} - 1) \Big|_{v_{r1}}^{v_{r2}} \quad (40)$$

Assuming a rupture with zero initial and final rupture speeds, the right side of this equation equals 0. The left side can be decomposed as

$$(\overline{G_0} - \overline{G_c}) WL - \Delta A (\overline{G_{cd}} - \overline{G_{0d}}) WL_d = 0 \quad (41)$$

where $L = L_2 - L_1$, $\overline{G_0}$ and $\overline{G_c}$ are the averaged values of potential and fracture energies along the whole rupture, L_d is the deceleration length, $\overline{G_{0d}}$ and $\overline{G_{cd}}$ are their averaged values in the deceleration portion, and $\Delta A = 1.2 - 1 = 0.2$ is the difference between the coefficients A for deceleration and acceleration. Since the energy release rate G_0 is also the static energy release, $(\overline{G_0} - \overline{G_c}) WL$ is the net energy difference between the total released and dissipated energies, which shall be equal to the total radiated energy E_r . This is also the first term on the right side of equation (41); thus, $E_r \approx \Delta A (\overline{G_{cd}} - \overline{G_{0d}}) WL_d$.

Combining this result with equation (24), we can also write the radiated energy as $E_r \approx \Delta A / A_d (\overline{G_{0a}} - \overline{G_{ca}}) W L_a$, where $\overline{G_{0a}}$ and $\overline{G_{ca}}$ are the averaged values in the acceleration portion, L_a is the acceleration length, and $\Delta A / A_d = 0.17$. Note that the radiated energy is proportional to ΔA : the difference of the coefficients A involved in the equation-of-motion for rupture acceleration and deceleration is related to seismic radiation.

5. Conclusions

Earthquake rupture propagation along elongated faults has been investigated by combining analytical and numerical methods, based on 2.5-D and 3-D dynamic rupture models. We developed a rupture-tip-equation-of-motion, a theoretical relation that links the evolution of rupture speed and the along-strike distribution of fault stress, fracture energy, and rupture width. The equation has the form $W' / v_s^2 / (1 - G_c / G_0) \dot{v}_r = A \alpha_s^P$, where $A = 1$ and $P = 3$ for rupture acceleration and $A = 1.2$ and $P = 2.6$ for rupture deceleration. In contrast to the classical crack-tip-equation-of-motion in 2D, the equation for 3-D ruptures with bounded width features an “inertial effect”; that is, it depends explicitly on the rupture acceleration. This makes long ruptures in 3D less reactive to fault heterogeneities than in 2D.

The energy release rate of a long steady state rupture depends on rupture width, stress drop, and shear modulus, and is independent of propagation distance and rupture speed. If the energy release rate is exactly balanced by the fracture energy, the rupture can in principle propagate in steady state at any speed. The stability of steady state ruptures depends on the rate dependency of fracture energy. If the fracture energy is constant or speed weakening, steady state ruptures are destabilized by small perturbations. In contrast, speed-strengthening fracture energy can stabilize the steady state ruptures. Fast steady ruptures are more stable than slow steady ruptures.

The fundamental rupture-tip-equation-of-motion provides a link between the kinematics and dynamics of elongated ruptures: it leads to theoretical relations between earthquake source properties and the heterogeneities of stress and strength along the fault. Within this framework, we defined a nondimensional rupture potential on a segmented fault system that quantifies the possibility of multisegment ruptures and thus may contribute to physics-based hazard assessment. The rupture-tip-equation-of-motion also provides simple theoretical relations between earthquake source properties (time-dependent features) and the heterogeneities of stress and strength along the fault, which could enable to extract statistical or scaling information of fault properties from global past earthquakes and to provide physics-based constraints on finite-fault source inversion.

Appendix A.

A.1. Governing Equations of the 2.5-D Antiplane Model

A.1.1. Elsasser's model

The Elsasser's 2.5-D model accounts approximately for a finite seismogenic layer W by averaging stresses and displacements across the entire seismogenic layer W :

$$\overline{\sigma}_{ij}(x_1, x_2, t) = \frac{1}{W} \int_{-W}^0 \sigma_{ij}(x_1, x_2, x_3, t) dx_3 \quad (42)$$

$$\overline{u}_i(x_1, x_2, t) = \frac{1}{W} \int_{-W}^0 u_i(x_1, x_2, x_3, t) dx_3 \quad (43)$$

where $i = 1, 2, 3$ and $j = 1, 2$. The depth-averaged momentum equation is

$$\overline{\sigma}_{ij,j} - \tau_i / W = \rho \ddot{u}_i \quad (44)$$

where ρ is the density of the material and $\tau_i = \sigma_{3i}(x_1, x_2, -W, t)$ are the resistance of the media outside the seismogenic layer to a sudden displacement \overline{u}_i on each horizontal location of the seismogenic layer (Lehner et al., 1981; Rice, 1980). We assume that τ_i is also averaged uniformly across the entire seismogenic layer, that is, τ_i / W . This model is the same as the elastic lithospheric and viscoelastic asthenosphere model (Lehner et al., 1981; Rice, 1980), but only accounting for the coseismic deformation; that is, the viscosity of

the asthenosphere layer does not play a role at short coseismic time scales. We consider pure dip-slip faulting and, for simplicity, we further assume that all displacements are vertical. This assumption reduces the system of differential equations to a single differential equation ($i = 3$). Using the relation between shear stress and displacement given by Hooke's law,

$$\bar{\sigma}_{3j} = \mu \frac{\partial \bar{u}_3}{\partial x_j} \quad (45)$$

where μ is the shear modulus, we get

$$\mu \left(\frac{\partial^2 \bar{u}_3}{\partial x_1^2} + \frac{\partial^2 \bar{u}_3}{\partial x_2^2} \right) - \frac{\tau_3}{W} = \rho \ddot{\bar{u}}_3 \quad (46)$$

The relation between τ_3 and \bar{u}_3 can be similarly given as (Lehner et al., 1981; Rice, 1980)

$$\tau_3 = \frac{\mu \bar{u}_3}{\gamma^2 W} \quad (47)$$

where γ is a geometric factor. Replace \bar{u}_3 with u , then the governing equation is

$$\frac{\partial^2 u}{\partial x_1^2} + \frac{\partial^2 u}{\partial x_2^2} - \frac{u}{(\gamma W)^2} = \frac{1}{v_s^2} \frac{\partial^2 u}{\partial t^2} \quad (48)$$

where $v_s = \sqrt{\mu/\rho}$ is the S wave speed. Lehner et al. (1981) proposed $\gamma = \pi/4$ such that on an infinitely long rupture with uniform stress drop the depth-averaged slip given by the 2.5-D model agrees with the slip obtained from known crack solutions on a vertical 2-D cross-section plane. Based on the comparison between 2.5-D and 3-D dynamic simulations, we suggest that $\gamma = 1/\pi$ for a deeply buried fault and $\gamma = 2/\pi$ for a shallow fault on a half-space such that their definitions of energy release rate are the same, $G_0 = \gamma \Delta \tau^2 W / \mu$.

A.1.2. Fourier Transform Analogy

Equation (48) can be derived by an alternative approach, leading to a different interpretation of the coefficient γ . The approach is similar to the 2.5-D formulation of wave propagation in 3-D media with 2-D varying structure under obliquely incident plane waves based on Fourier transform along the invariant axis (e.g., Takenaka & Kennett, 1996). Consider, for the sake of simplicity, a scalar wave equation involving only S waves:

$$\frac{\partial^2 u}{\partial x_1^2} + \frac{\partial^2 u}{\partial x_2^2} + \frac{\partial^2 u}{\partial x_3^2} = \frac{1}{v_s^2} \frac{\partial^2 u}{\partial t^2} \quad (49)$$

The slip on a deeply buried fault with relatively uniform stress drop has a semielliptical depth profile, which can be approximated as one half of a cosine of wavelength $2W$. We crudely assume that the whole displacement field can be represented by a sinusoidal depth profile of wavelength $2W$, as $u(x_1, x_2, t) e^{ik_3 x_3}$ with $k_3 = \pi/W$. Based on this ansatz, equation (49) leads to equation (48) with $\gamma = 1/\pi$. In a shallow fault on a half-space, the slip is maximal at the surface and zero at the bottom of the rupture and the depth profile can be approximated as one quarter of a cosine of wavelength $4W$, which leads to $\gamma = 2/\pi$. Taking these two cases as end-members, for a buried fault we expect γ to take values between $1/\pi$ and $2/\pi$.

A.2. Derivation of the $K_{III}(v_r)$ Function

Referring to Freund (1998), we introduce a reference frame that propagates with the crack tip along the x_1 axis at the velocity v_r and assume $u(x_1, x_2, t) = u(\xi, \eta)$, where $\xi = x_1 - v_r t$ and $\eta = x_2$. Then we have

$$\frac{\partial^2 u}{\partial x_1^2} = \frac{\partial^2 u}{\partial \xi^2} \quad (50)$$

$$\frac{\partial^2 u}{\partial l^2} = \nu_r^2 \frac{\partial^2 u}{\partial \xi^2} \quad (51)$$

The governing equation can be written as

$$\alpha_s^2 \frac{\partial^2 u}{\partial \xi^2} + \frac{\partial^2 u}{\partial \eta^2} - \frac{u}{(\gamma W)^2} = 0 \quad (52)$$

where $\alpha_s = \sqrt{1 - (\nu_r/\nu_s)^2}$. The boundary condition of a semiinfinite crack is

$$\begin{aligned} u(\xi, 0) &= 0 & \xi > L \\ \frac{\mu \partial u}{\partial \eta} &= -\Delta\tau & 0 < \xi < L \\ \frac{\mu \partial u}{\partial \eta} &= 0 & \xi < 0 \\ \partial u / \partial \xi, \partial u / \partial \eta &\rightarrow 0 & \xi^2 + \eta^2 \rightarrow \infty \end{aligned} \quad (53)$$

where $\Delta\tau$ is the prescribed stress drop. The above equations are similar to equations (56) and (57) in Lehner et al. (1981) (assuming the viscosity equals 0). By replacing $(1+\nu)^2$ with α_s^2 , $\beta^{1/2}$ with γW , q with $\Delta\tau$, and letting $\alpha = 0$ in those equations, we obtain the following stress intensity factor:

$$K_{III}(\nu_r) = \Delta\tau [2\gamma W \alpha_s]^{1/2} \cdot \text{erf} \left\{ \left[\frac{1-L}{\alpha_s \gamma W} \right]^{1/2} \right\} \quad (54)$$

where erf is the error function. Similarly, we can also obtain a general solution of steady stress intensity factor for a variable stress drop $\Delta\tau(x)$ along $x < L$:

$$K_{III}(\nu_r) = \sqrt{\frac{2}{\pi}} \int_{-\infty}^L \frac{\Delta\tau(\xi)}{(L-\xi)^{1/2}} e^{\frac{\xi-L}{W\alpha_s}} d\xi \quad (55)$$

where the weighting function decays sharply and $K_{III}(\nu_r)$ is mainly controlled by the value of $\Delta\tau(x)$ shortly behind the rupture tip.

A.3. Derivation of the $g(\nu_r)$ Function

We rewrite equation (52) as

$$\alpha_s^2 \frac{\partial^2 u}{\partial x^2} + \frac{\partial^2 u}{\partial y^2} - \frac{u}{(\gamma W)^2} = 0 \quad (56)$$

We rescale the coordinate system by assuming that $\xi = x$ and $\eta = \alpha_s y$, then

$$\frac{\partial^2 u}{\partial \xi^2} + \frac{\partial^2 u}{\partial \eta^2} - \frac{u}{(\alpha_s \gamma W)^2} = 0 \quad (57)$$

Switching equation (57) to polar coordinates (r_s, θ_s)

$$\frac{\partial^2 u}{\partial r_s^2} + \frac{1}{r_s} \frac{\partial u}{\partial r_s} + \frac{1}{r_s^2} \frac{\partial^2 u}{\partial \theta_s^2} = \frac{u}{(\alpha_s \gamma W)^2} \quad (58)$$

where $r_s = \sqrt{x^2 + \alpha_s^2 y^2}$ and $\tan \theta_s = \alpha_s y/x$. Assuming that the function $u(r_s, \theta_s)$ has the form

$$u(r_s, \theta_s) = \Sigma(\theta_s) \sqrt{r_s} \quad (59)$$

we convert equation (58) to

$$\Sigma''(\theta_s) + \frac{1}{4}\Sigma(\theta_s) = r_s^{\frac{3}{2}} \frac{u}{(\alpha_s \gamma W)^2} \quad (60)$$

To derive the asymptotics of stress near the crack tip, we let $r_s \rightarrow 0$, and the right side of equation (60) vanishes. Considering the boundary condition $\Sigma(0) = 0$, the approximated displacement field near the tip is

$$u(r_s, \theta_s) \approx 2Q\sqrt{r_s} \sin \frac{1}{2}\theta_s \quad (61)$$

where Q is an undetermined parameter. According to the stress-strain relation of elastic materials and half-angle formulas we have

$$\Delta\sigma_{13} = \mu \frac{\partial u}{\partial x} = -\frac{Q\mu}{\sqrt{r_s}} \sin \frac{1}{2}\theta_s \quad (62)$$

$$\Delta\sigma_{23} = \mu \frac{\partial u}{\partial y} = \frac{Q\mu\alpha_s}{\sqrt{r_s}} \cos \frac{1}{2}\theta_s \quad (63)$$

The stress intensity factor for mode III is defined by taking the limit of the function for $y = 0$ (or $\theta_s = 0$)

$$K_{III}(v_r) = \lim_{x \rightarrow 0^+} \sqrt{2\pi x} \cdot \Delta\sigma_{23} \quad (64)$$

then

$$Q = K_{III}(v_r) / (\mu\alpha_s \sqrt{2\pi}) \quad (65)$$

Referring to the definition of the functions $\Sigma_{ij}^{III}(\theta, v_r)$ for the 2.5-D mode III model (equation (6)) are

$$\Sigma_{13}^{III}(\theta, v_r) = -\frac{\sin \frac{1}{2}\theta_s}{\alpha_s \sqrt{\gamma_s}} \quad (66)$$

$$\Sigma_{23}^{III}(\theta, v_r) = \frac{\cos \frac{1}{2}\theta_s}{\sqrt{\gamma_s}} \quad (67)$$

where $\gamma_s = r_s/r = \sqrt{1 - (v_r \sin\theta/v_s)^2}$, $r = \sqrt{x^2 + y^2}$, and $\tan\theta = y/x$. The $\Sigma_{ij}^{III}(\theta, v_r)$ of 2.5-D model are exactly the same as those of the 2-D model (Freund, 1998).

Equation (52) can be written as conservation of momentum

$$\sigma_{ij,j} - \frac{\mu u_i}{(\gamma W)^2} = \rho \frac{\partial^2 u_i}{\partial t^2} \quad (68)$$

In order to obtain the $g(v_r)$ function, we write the inner product of equation (68) with the particle velocity $\partial u_i / \partial t$ as

$$\frac{\partial}{\partial x_j} \left(\sigma_{ij} \frac{\partial u_i}{\partial t} \right) - \frac{\partial}{\partial t} (U + T + F) = 0 \quad (69)$$

where U is the stress work density, T is the kinetic energy density, and F is the work acted by the bottom of the seismogenic layer, that is

$$\begin{aligned}
 U &= \int_{-\infty}^t \sigma_{ij} \frac{\partial^2 u_i}{\partial t' \partial x_j} dt' \\
 T &= \frac{1}{2} \rho \frac{\partial u_i}{\partial t} \frac{\partial u_i}{\partial t} \\
 F &= \frac{1}{2} \frac{\mu u_i}{(\gamma W)^2} u_i
 \end{aligned} \tag{70}$$

where the term $\mu u_i / (\gamma W)^2$ acts as a body force. The dynamic energy release rate G , the rate of mechanical energy flow into the crack tip per unit crack advance, can be written as

$$G = \lim_{\Gamma \rightarrow 0} \left\{ \frac{1}{v_r} \int_{\Gamma} \left[\sigma_{ij} n_j \frac{\partial u_i}{\partial t} + (U + T + F) v_r n_1 \right] d\Gamma \right\} \tag{71}$$

where the contour Γ is a closed curve shrinking onto the crack tip and n_i is the unit normal vector to Γ . The difference between this equation and that of the 2-D model in Freund (1998) is the term F . Choosing the contour Γ to be a rectangle, with length $2\delta_1$ parallel to the x axis and width $2\delta_2$ parallel to the y axis, and letting $\delta_2 \rightarrow 0$ first and then $\delta_1 \rightarrow 0$, the second term in the right side of equation (71) vanishes. Thus, the evaluation of G for the 2.5-D model is the same as that of the 2-D model and $g(v_r)$ has the form

$$g(v_r) = \frac{1}{\alpha_s} \tag{72}$$

Acknowledgments

Acknowledgments The open-source software SPECFEM3D used in our 3-D dynamic rupture simulations is available from the Computational Infrastructure for Geodynamics at <https://geodynamics.org/cig/software/specfem3d/>. We express our deepest gratitude in memory of Dimitri Komatitsch, whose pioneering work on the spectral element method in seismology and generous development of SPECFEM3D enabled a whole generation of computational seismology studies, including ours. The open-source software SEMLAB for 2.5-D dynamic rupture simulations based on the spectral element method is available at <https://github.com/jpampuero/semlab>. The SPECFEM3D simulations were conducted in the Cluster THERA in Géoazur. This work was supported by the French government through the Investments in the Future project UCAJEDI (ANR-15-IDEX-01) managed by the French National Research Agency (ANR). J.P. A. acknowledges partial funding from NAM (Nederlandse Aardolie Maatschappij). All data of dynamic models are generated from numerical simulations. All figures are produced by using Generic Mapping Tools (GMT). We benefited from discussions with Robert Viesca, M.P.A. van den Ende, and Hongfeng Yang. We thank Eric Dunham and Raul Madariaga for their informative reviews.

References

- Ader, T., Avouac, J. P., Liu-Zeng, J., Lyon-Caen, H., Bollinger, L., Galetzka, J., et al. (2012). Convergence rate across the Nepal Himalaya and interseismic coupling on the Main Himalayan Thrust: Implications for seismic hazard. *Journal of Geophysical Research*, *117*, B04403. <https://doi.org/10.1029/2011JB009071>
- Aki, K., & Richards, P. G. (2002). *Quantitative seismology*. Sausalito, CA: University Science Books.
- Ammon, C. J., Ji, C., Thio, H.-K., Robinson, D., Ni, S., Hjorleifsdottir, V., et al. (2005). Rupture process of the 2004 Sumatra-Andaman earthquake. *Science*, *308*(5725), 1133–1139. <https://doi.org/10.1126/science.1112260>
- Ampuero, J. (2002). Etude physique et numérique de la nucléation des séismes, *PhD Thesis, University of Paris VII, France*.
- Ampuero, J., & Ben-Zion, Y. (2008). Cracks, pulses and macroscopic asymmetry of dynamic rupture on a bimaterial interface with velocity-weakening friction. *Geophysical Journal International*, *173*(2), 674–692. <https://doi.org/10.1111/j.1365-246X.2008.03736.x>
- Ampuero, J., & Mao, X. (2017). Upper limit on damage zone thickness controlled by seismogenic depth. In *Fault zone dynamic processes: Evolution of fault properties during seismic rupture*, (Vol. 227, Chap. 13, pp. 243–253). Washington, DC: American Geophysical Union.
- Ampuero, J., & Rubin, A. M. (2008). Earthquake nucleation on rate and state faults: Aging and slip laws. *Journal of Geophysical Research*, *113*, B01302. <https://doi.org/10.1029/2007JB005082>
- Andrews, D. J. (1976a). Rupture propagation with finite stress in antiplane strain. *Journal of Geophysical Research*, *81*(20), 3575–3582. <https://doi.org/10.1029/JB081i020p03575>
- Andrews, D. J. (1976b). Rupture velocity of plane strain shear cracks. *Journal of Geophysical Research*, *81*(32), 5679–5687. <https://doi.org/10.1029/JB081i032p05679>
- Andrews, D. J. (1985). Dynamic plane-strain shear rupture with a slip-weakening friction law calculated by a boundary integral method. *Bulletin of the Seismological Society of America*, *75*(1), 1–21.
- Andrews, D. J. (2005). Rupture dynamics with energy loss outside the slip zone. *Journal of Geophysical Research*, *110*, B01307. <https://doi.org/10.1029/2004JB003191>
- Avouac, J.-P., Meng, L., Wei, S., Wang, T., & Ampuero, J.-P. (2015). Lower edge of locked Main Himalayan Thrust unzipped by the 2015 Gorkha earthquake. *Nature Geoscience*, *8*(9), 708–711. <https://doi.org/10.1038/ngeo2518>
- Bai, K., & Ampuero, J. P. (2017). Effect of seismogenic depth and background stress on physical limits of earthquake rupture across fault step overs. *Journal of Geophysical Research: Solid Earth*, *122*, 10,280–10,298. <https://doi.org/10.1002/2017JB014848>
- Bao, H., Ampuero, J.-P., Meng, L., Fielding, E. J., Liang, C., Milliner, C. W. D., et al. (2019). Early and persistent supershear rupture of the 2018 magnitude 7.5 Palu earthquake. *Nature Geoscience*, *12*(3), 200–205. <https://doi.org/10.1038/s41561-018-0297-z>
- Buijze, L., van den Bogert, P., Wassing, B. B. T., & Orlic, B. (2019). Nucleation and arrest of dynamic rupture induced by reservoir depletion. *Journal of Geophysical Research: Solid Earth*, *124*, 3620–3645. <https://doi.org/10.1029/2018JB016941>
- Burridge, R. (1973). Admissible speeds for plane-strain self-similar shear cracks with friction but lacking cohesion. *Geophysical Journal International*, *35*(4), 439–455. <https://doi.org/10.1111/j.1365-246X.1973.tb00608.x>
- Carlson, J. M., Langer, J. S., & Shaw, B. E. (1994). Dynamics of earthquake faults. *Reviews of Modern Physics*, *66*(2), 657–670. <https://doi.org/10.1103/RevModPhys.66.657>
- Custódio, S., Liu, P., & Archuleta, R. J. (2005). The 2004 M_w 6.0 Parkfield, California, earthquake: Inversion of near-source ground motion using multiple data sets. *Geophysical Research Letters*, *32*, L23312. <https://doi.org/10.1029/2005GL024417>
- Dalguer, L. A., & Day, S. M. (2009). Asymmetric rupture of large aspect-ratio faults at bimaterial interface in 3D. *Geophysical Research Letters*, *36*, L23307. <https://doi.org/10.1029/2009GL040303>
- Day, S. M. (1982). Three-dimensional finite difference simulation of fault dynamics: Rectangular faults with fixed rupture velocity. *Bulletin of the Seismological Society of America*, *72*(3), 705–727.
- Day, S. M., Dalguer, L. A., Lapusta, N., & Liu, Y. (2005). Comparison of finite difference and boundary integral solutions to three-dimensional spontaneous rupture. *Journal of Geophysical Research*, *110*, B12307. <https://doi.org/10.1029/2005JB003813>

- Denolle, M. A., & Shearer, P. M. (2016). New perspectives on self-similarity for shallow thrust earthquakes. *Journal of Geophysical Research: Solid Earth*, *121*, 6533–6565. <https://doi.org/10.1002/2016JB013105>
- Freund, L. (1979). The mechanics of dynamic shear crack propagation. *Journal of Geophysical Research*, *84*(B5), 2199–2209. <https://doi.org/10.1029/JB084iB05p02199>
- Freund, L. (1998). *Dynamic fracture mechanics*. Cambridge: Cambridge University Press.
- Gabriel, A. A., Ampuero, J. P., Dalguer, L., & Mai, P. M. (2013). Source properties of dynamic rupture pulses with off-fault plasticity. *Journal of Geophysical Research: Solid Earth*, *118*, 4117–4126. <https://doi.org/10.1002/jgrb.50213>
- Galis, M., Ampuero, J. P., Mai, P. M., & Cappa, F. (2017). Induced seismicity provides insight into why earthquake ruptures stop. *Science Advances*, *3*(12), eaap7528. <https://doi.org/10.1126/sciadv.aap7528>
- Galis, M., Ampuero, J.-P., Mai, P. M., & Kristek, J. (2018). Initiation and arrest of earthquake ruptures due to elongated overstressed regions. *Geophysical Journal International*, *217*(3), 1783–1797. <https://doi.org/10.1093/gji/ggz086/5322168>
- Galvez, P., Ampuero, J.-P., Dalguer, L. A., Somala, S. N., & Nissen-Meyer, T. (2014). Dynamic earthquake rupture modelled with an unstructured 3-D spectral element method applied to the 2011 *M* 9 Tohoku earthquake. *Geophysical Journal International*, *198*(2), 1222–1240. <https://doi.org/10.1093/gji/ggu203>
- Goldman, T., Livne, A., & Fineberg, J. (2010). Acquisition of inertia by a moving crack. *Physical Review Letters*, *104*(11), 114301. <https://doi.org/10.1103/PhysRevLett.104.114301>
- Gomberg, J., Wech, A., Creager, K., Obara, K., & Agnew, D. (2016). Reconsidering earthquake scaling. *Geophysical Research Letters*, *43*, 6243–6251. <https://doi.org/10.1002/2016GL069967>
- Harris, R. A. (2017). Large earthquakes and creeping faults. *Reviews of Geophysics*, *55*, 169–198. <https://doi.org/10.1002/2016RG000539>
- Haskell, N. (1964). Total energy and energy spectral density of elastic wave radiation from propagating faults. *Bulletin of the Seismological Society of America*, *54*(6A), 1811–1841.
- Heimpel, M. (2003). Characteristic scales of earthquake rupture from numerical models. *Nonlinear Processes in Geophysics*, *10*(6), 573–584. <https://doi.org/10.5194/npg-10-573-2003>
- Henry, C., & Das, S. (2001). Aftershock zones of large shallow earthquakes: Fault dimensions, aftershock area expansion and scaling relations. *Geophysical Journal International*, *147*(2), 272–293. <https://doi.org/10.1046/j.1365-246X.2001.00522.x>
- Ida, Y. (1972). Cohesive force across the tip of a longitudinal-shear crack and Griffith's specific surface energy. *Journal of Geophysical Research*, *77*(20), 3796–3805. <https://doi.org/10.1029/JB077i020p03796>
- Imanishi, K., & Ellsworth, W. L. (2006). Source scaling relationships of microearthquakes at Parkfield, CA, determined using the SAFOD pilot hole seismic array. In *Earthquakes: Radiated Energy and the Physics of Faulting, Geophysical Monograph Series* (Vol. 170, pp. 81–90). Washington, DC: American Geophysical Union.
- Ishii, M., Shearer, P. M., Houston, H., & Vidale, J. E. (2005). Extent, duration and speed of the 2004 Sumatra–Andaman earthquake imaged by the Hi-Net array. *Nature*, *435*(7044), 933–936. <https://doi.org/10.1038/nature03675>
- Johnson, E. (1992). The influence of the lithospheric thickness on bilateral slip. *Geophysical Journal International*, *108*(1), 151–160. <https://doi.org/10.1111/j.1365-246X.1992.tb00846.x>
- Kammer, D. S., Svetlizky, I., Cohen, G., & Fineberg, J. (2018). The equation of motion for supershear frictional rupture fronts. *Science Advances*, *4*(7), eaat5622. <https://doi.org/10.1126/sciadv.aat5622>
- Kanamori, H., & Anderson, D. L. (1975). Theoretical basis of some empirical relations in seismology. *Bulletin of the Seismological Society of America*, *65*(5), 1073–1095.
- Kaneko, Y., Avouac, J.-P., & Lapusta, N. (2010). Towards inferring earthquake patterns from geodetic observations of interseismic coupling. *Nature Geoscience*, *3*(5), 363–369. <https://doi.org/10.1038/ngeo843>
- Kaneko, Y., & Lapusta, N. (2008). Variability of earthquake nucleation in continuum models of rate-and-state faults and implications for aftershock rates. *Journal of Geophysical Research*, *113*, B12312. <https://doi.org/10.1029/2007JB005154>
- Kaneko, Y., Lapusta, N., & Ampuero, J. P. (2008). Spectral element modeling of spontaneous earthquake rupture on rate and state faults: Effect of velocity-strengthening friction at shallow depths. *Journal of Geophysical Research*, *113*, B09317. <https://doi.org/10.1029/2007JB005553>
- Karimzadeh, S., Kahir, Z., Osmanoglu, B., Schmalzle, G., Miyajima, M., Amiraslanzadeh, R., & Djamour, Y. (2013). Interseismic strain accumulation across the North Tabriz Fault (NW Iran) deduced from InSAR time series. *Journal of Geodynamics*, *66*(0), 53–58. <https://doi.org/10.1016/j.jog.2013.02.003>
- Klinger, Y. (2010). Relation between continental strike-slip earthquake segmentation and thickness of the crust. *Journal of Geophysical Research*, *115*, B07306. <https://doi.org/10.1029/2009JB006550>
- Komatitsch, D., & Vilotte, J.-P. (1998). The spectral element method: An efficient tool to simulate the seismic response of 2D and 3D geological structures. *Bulletin of the Seismological Society of America*, *88*(2), 368–392.
- Kostrov, B. (1964). Self-similar problems of propagation of shear cracks. *Journal of Applied Mathematics and Mechanics*, *28*(5), 1077–1087. [https://doi.org/10.1016/0021-8928\(64\)90010-3](https://doi.org/10.1016/0021-8928(64)90010-3)
- Langer, J., Carlson, J., Myers, C. R., & Shaw, B. E. (1996). Slip complexity in dynamic models of earthquake faults. *Proceedings of the National Academy of Sciences*, *93*(9), 3825–3829. <https://doi.org/10.1073/pnas.93.9.3825>
- Lapusta, N. (2001). Elastodynamic analyses of sliding with rate and state friction. (PhD thesis). Harvard University.
- Lehner, F. K., Li, V. C., & Rice, J. (1981). Stress diffusion along rupturing plate boundaries. *Journal of Geophysical Research*, *86*(B7), 6155–6169. <https://doi.org/10.1029/JB086iB07p06155>
- Luo, Y., J.-P. Ampuero, K. Miyakoshi, & K. Irikura (2017). Surface rupture effects on earthquake moment-area scaling relations. *Pure and Applied Geophysics*, *174*(9), 3331–3342. <https://doi.org/10.1007/s00024-017-1467-4>
- Madariaga, R. (1977). High-frequency radiation from crack (stress drop) models of earthquake faulting. *Geophysical Journal International*, *51*(3), 625–651. <https://doi.org/10.1111/j.1365-246X.1977.tb04211.x>
- Madariaga, R. (1983). High frequency radiation from dynamic earthquake fault models. *Annales Geophysicae*, *1*(1), 17–23.
- Madariaga, R., Ampuero, J., & Adda-Bedia, M. (2006). Seismic radiation from simple models of earthquakes. In *Earthquakes: Radiated energy and the physics of faulting, Geophysical Monograph Series* (Vol. 170, pp. 223–236). Washington, DC: American Geophysical Union.
- Madariaga, R., & Olsen, K. B. (2000). Criticality of rupture dynamics in 3-D. *Pure and Applied Geophysics*, *157*(11), 1981–2001. <https://doi.org/10.1007/PL00001071>
- Mai, P. M., & Thingbaijam, K. (2014). SRCMOD: An online database of finite-fault rupture models. *Seismological Research Letters*, *85*(6), 1348–1357. <https://doi.org/10.1785/0220140077>
- Marder, M. (1998). Adiabatic equation for cracks. *Philosophical Magazine B*, *78*(2), 203–214. <https://doi.org/10.1080/13642819808202942>

- Meier, M.-A., Ampuero, J., & Heaton, T. (2017). The hidden simplicity of subduction megathrust earthquakes. *Science*, 357(6357), 1277–1281. <https://doi.org/10.1126/science.aan5643>
- Mello, M., Bhat, H., Rosakis, A., & Kanamori, H. (2014). Reproducing the supershear portion of the 2002 Denali earthquake rupture in laboratory. *Earth and Planetary Science Letters*, 387, 89–96. <https://doi.org/10.1016/j.epsl.2013.11.030>
- Metois, M., Socquet, A., & Vigny, C. (2012). Interseismic coupling, segmentation and mechanical behavior of the central Chile subduction zone. *Journal of Geophysical Research*, 117, B03406. <https://doi.org/10.1029/2011JB008736>
- Michailos, K., Smith, E. G., Chamberlain, C. J., Savage, M. K., & Townend, J. (2019). Variations in seismogenic thickness along the Central Alpine Fault, New Zealand, revealed by a decade's relocated microseismicity. *Geochemistry, Geophysics, Geosystems*, 20, 470–486. <https://doi.org/10.1029/2018GC007743>
- Michel, S., Avouac, J. P., Lapusta, N., & Jiang, J. (2017). Pulse-like partial ruptures and high-frequency radiation at creeping-locked transition during megathrust earthquakes. *Geophysical Research Letters*, 44, 8345–8351. <https://doi.org/10.1002/2017GL074725>
- Myers, C. R., Shaw, B. E., & Langer, J. S. (1996). Slip complexity in a crustal-plane model of an earthquake fault. *Physical Review Letters*, 77(5), 972–975. <https://doi.org/10.1103/PhysRevLett.77.972>
- Nielsen, S., & Madariaga, R. (2003). On the self-healing fracture mode. *Bulletin of the Seismological Society of America*, 93(6), 2375–2388. <https://doi.org/10.1785/0120020090>
- Noda, H., & Lapusta, N. (2013). Stable creeping fault segments can become destructive as a result of dynamic weakening. *Nature*, 493(7433), 518–521. <https://doi.org/10.1038/nature11703>
- Okuda, T., & Ide, S. (2018). Streak and hierarchical structures of the Tohoku–Hokkaido subduction zone plate boundary. *Earth, Planets and Space*, 70(1), 132. <https://doi.org/10.1186/s40623-018-0903-8>
- Perfettini, H., Avouac, J.-P., Tavera, H., Kositsky, A., Nocquet, J.-M., Bondoux, F., et al. (2010). Seismic and aseismic slip on the central Peru megathrust. *Nature*, 465(7294), 78–81. <https://doi.org/10.1038/nature09062>
- Rice, J. (1980). The mechanics of earthquake rupture. In A. M. Dziewonski, & E. Boschi (Eds.), *Physics of the Earth's interior, Proc. Internat. School of Physics Soc. Enrico Fermi, Course 78, 1979*, (pp. 555–649). North Holland, Amsterdam: Italian Physical Society.
- Rice, J. (2006). Heating and weakening of faults during earthquake slip. *Journal of Geophysical Research*, 111, B05311. <https://doi.org/10.1029/2005JB004006>
- Rice, J., Sammis, C. G., & Parsons, R. (2005). Off-fault secondary failure induced by a dynamic slip pulse. *Bulletin of the Seismological Society of America*, 95(1), 109–134. <https://doi.org/10.1785/0120030166>
- Rubin, A., & Ampuero, J. P. (2005). Earthquake nucleation on (aging) rate and state faults. *Journal of Geophysical Research*, 110, B11312. <https://doi.org/10.1029/2005JB003686>
- Savage, J. (1972). Relation of corner frequency to fault dimensions. *Journal of Geophysical Research*, 77(20), 3788–3795. <https://doi.org/10.1029/JB077i020p03788>
- Shaw, B. E. (2004). Self-organizing fault systems and self-organizing elastodynamic events on them: Geometry and the distribution of sizes of events. *Geophysical Research Letters*, 31, L17603. <https://doi.org/10.1029/2004GL019726>
- Smith-Konter, B. R., Sandwell, D. T., & Shearer, P. (2011). Locking depths estimated from geodesy and seismology along the San Andreas Fault system: Implications for seismic moment release. *Journal of Geophysical Research*, 116, B06401. <https://doi.org/10.1029/2010JB008117>
- Spyropoulos, C., Scholz, C. H., & Shaw, B. E. (2002). Transition regimes for growing crack populations. *Physical Review E*, 65(5), 056105. <https://doi.org/10.1103/PhysRevE.65.056105>
- Svetlizky, I., & Fineberg, J. (2014). Classical shear cracks drive the onset of dry frictional motion. *Nature*, 509(7499), 205–208. <https://doi.org/10.1038/nature13202>
- Svetlizky, I., Kammer, D. S., Bayart, E., Cohen, G., & Fineberg, J. (2017). Brittle fracture theory predicts the equation of motion of frictional rupture fronts. *Physical Review Letters*, 118(12), 125501. <https://doi.org/10.1103/PhysRevLett.118.125501>
- Takenaka, H., & Kennett, B. L. (1996). A 2.5-D time-domain elastodynamic equation for plane-wave incidence. *Geophysical Journal International*, 125(2), 5–9. <https://doi.org/10.1111/j.1365-246X.1996.tb00001.x>
- Uchide, T., & Ide, S. (2010). Scaling of earthquake rupture growth in the Parkfield area: Self-similar growth and suppression by the finite seismogenic layer. *Journal of Geophysical Research*, 115, B11302. <https://doi.org/10.1029/2009JB007122>
- Uchide, T., & Imanishi, K. (2016). Small earthquakes deviate from the omega-square model as revealed by multiple spectral ratio analysis. *Bulletin of the Seismological Society of America*, 106(3), 1357–1363. <https://doi.org/10.1785/0120150322>
- Vallée, M., Charléty, J., Ferreira, A. M., Delouis, B., & Vergoz, J. (2011). SCARDEC: A new technique for the rapid determination of seismic moment magnitude, focal mechanism and source time functions for large earthquakes using body-wave deconvolution. *Geophysical Journal International*, 184(1), 338–358. <https://doi.org/10.1111/j.1365-246X.2010.04836.x>
- Viesca, R. C., & Garagash, D. I. (2015). Ubiquitous weakening of faults due to thermal pressurization. *Nature Geoscience*, 8(11), 875–879. <https://doi.org/10.1038/ngeo2554>
- Wang, D., Mori, J., & Koketsu, K. (2016). Fast rupture propagation for large strike-slip earthquakes. *Earth and Planetary Science Letters*, 440, 115–126. <https://doi.org/10.1016/j.epsl.2016.02.022>
- Wang, Q., Xuejun, Q., Qigui, L., Freymueller, J., Shaomin, Y., Caijun, X., et al. (2011). Rupture of deep faults in the 2008 Wenchuan earthquake and uplift of the Longmen Shan. *Nature Geoscience*, 4(9), 634–640. <https://doi.org/10.1038/ngeo1210>
- Wei, S., Helmlinger, D., Zhan, Z., & Graves, R. (2013). Rupture complexity of the M_w 8.3 sea of okhotsk earthquake: Rapid triggering of complementary earthquakes? *Geophysical Research Letters*, 40, 5034–5039. <https://doi.org/10.1002/grl.50977>
- Wells, D. L., & Coppersmith, K. J. (1994). New empirical relationships among magnitude, rupture length, rupture width, rupture area, and surface displacement. *Bulletin of the Seismological Society of America*, 84(4), 974–1002.
- Weng, H., & Yang, H. (2017). Seismogenic width controls aspect ratios of earthquake ruptures. *Geophysical Research Letters*, 44, 2725–2732. <https://doi.org/10.1002/2016GL072168>